Article:

Magee, C. orcid.org/0000-0001-9836-2365, Ebmeier, S.K. and Hickey, J. (Accepted: 2025) Testing volcano deformation models against 3D seismic reflection imagery of ancient intrusions. Journal of Geophysical Research (JGR): Solid Earth. ISSN 2169-9313 (In Press)

Testing volcano deformation models against 3D seismic reflection imagery of ancient intrusions

Craig Magee[1]*, Susanna Ebmeier[1], James Hickey[2]

[1]School of Earth and Environment, University of Leeds, UK

[2]Department of Earth and Environmental Sciences, University of Exeter, UK

*Corresponding author: c.magee@leeds.ac.uk

Key points

1. Seismic reflection data images igneous intrusions and overlying host rock uplift (forced folding) in 3D
2. From a seismically imaged forced fold and laccolith, we derive syn-intrusion surface displacements to invert using analytical models
3. Modelled source positions and lateral dimensions broadly fit those of the observed laccolith, but emplacement depths differ

Abstract

Magma intrusion often drives uplift of the overburden and free surface. Analytical modelling of such surface uplift at active volcanoes allows us to estimate intrusion geometries, positions, and volume and pressure changes; these insights have proven critical to forecasting volcanic unrest and eruptions. However, it is rarely possible to compare geodetic source parameters retrieved from elastic half space inversions to known intrusion geometries. Seismic reflection data offer an opportunity to image and quantify ancient, buried intrusions geometries *and* their overburden deformation (i.e., a forced fold) in 3D. Here, we use 3D seismic reflection data offshore NW Australia to investigate an Early Cretaceous forced fold developed above a laccolith emplaced at ~0.6–1 km depth. We remove the effects of post-emplacement, burial-related compaction and derive possible surface displacement patterns for the forced fold. Analytical modelling of these surface displacements, using both thin plate bending and elastic half-space solutions, suggest source (intrusion) estimates of position and lateral dimensions are similar to those of the actual laccolith. There are some differences between measurements of the laccolith and modelled source estimates, which we attribute these to syn-intrusion space-making mechanisms (e.g., compaction). We particularly find penny shaped crack and rectangular dislocation elastic half-space solutions underestimate source emplacement depth by ~0.22–0.89 km, probably reflecting a lack of heterogeneity (layering) in our models. Our novel approach highlights seismic reflection data is a powerful tool for understanding and testing how magma emplacement translates into surface deformation at active volcanoes.

Plain language summary

As magma moves through the crust it pushes up overlying rock, causing the ground to move. We measure these tiny ground movements at active volcanoes and use computer models to predict how they relate to underlying magma body size and location; this provides us important information on whether an eruption may occur. However, the models we use are very simplistic and their results are very difficult to test. Here, we use 3D seismic reflection data, which provides ultrasound-like images of Earth's shallow subsurface, to study a buried, ancient magma body and the overlying rock it pushed upwards. We measure the amount of ground movement generated by the injecting magma. With the same computer models, we use these ground movement measurements to predict underlying magma body size and

location. Critically, our 3D seismic data allows us to compare these predicted magma body properties to the actual magma body. Our results show that the position and lateral dimensions of the predicted magma bodies are reasonable to that of the observed magma body. However, the predicted magma body depths are underestimated. Where we use these bodies at active volcanoes, we should thus be aware that the magma may actually be deeper than predicted.

1. Introduction

Space for emplacement of a new magma body, or recharge of an existing reservoir, can be generated by uplift of the overlying rock and free surface (e.g., Mogi, 1958; Pollard and Johnson, 1973; Hansen and Cartwright, 2006; Segall, 2010; Magee et al., 2017a; Karlstrom et al., 2018). The shape and magnitude of such surface displacement relates to the geometry, location, and conditions of the underlying magma intrusion and its host rock properties (e.g., Pollard and Johnson, 1973; Stearns, 1978; Segall, 2010; Galland and Scheibert, 2013). Surface displacements at active volcanoes typically have magnitudes of mm–m and occur over days-to-years (e.g., Segall, 2013; Biggs and Wright, 2020). By modelling measured surface displacement patterns at active volcanoes, we can estimate the subsurface source (intrusion) geometry, depth, volume change, and/or pressure change (e.g., Fig. 1A) (e.g., Lisowski, 2007; Masterlark et al., 2010; Segall, 2010; Sparks et al., 2012; Nikkhoo et al., 2016; Biggs and Wright, 2020). These modelled constraints on active volcanic domains are crucial for forecasting trajectories of unrest and eruption (e.g., Sparks, 2003; Ebmeier et al., 2018; Garthwaite et al., 2019; Crozier et al., 2023).

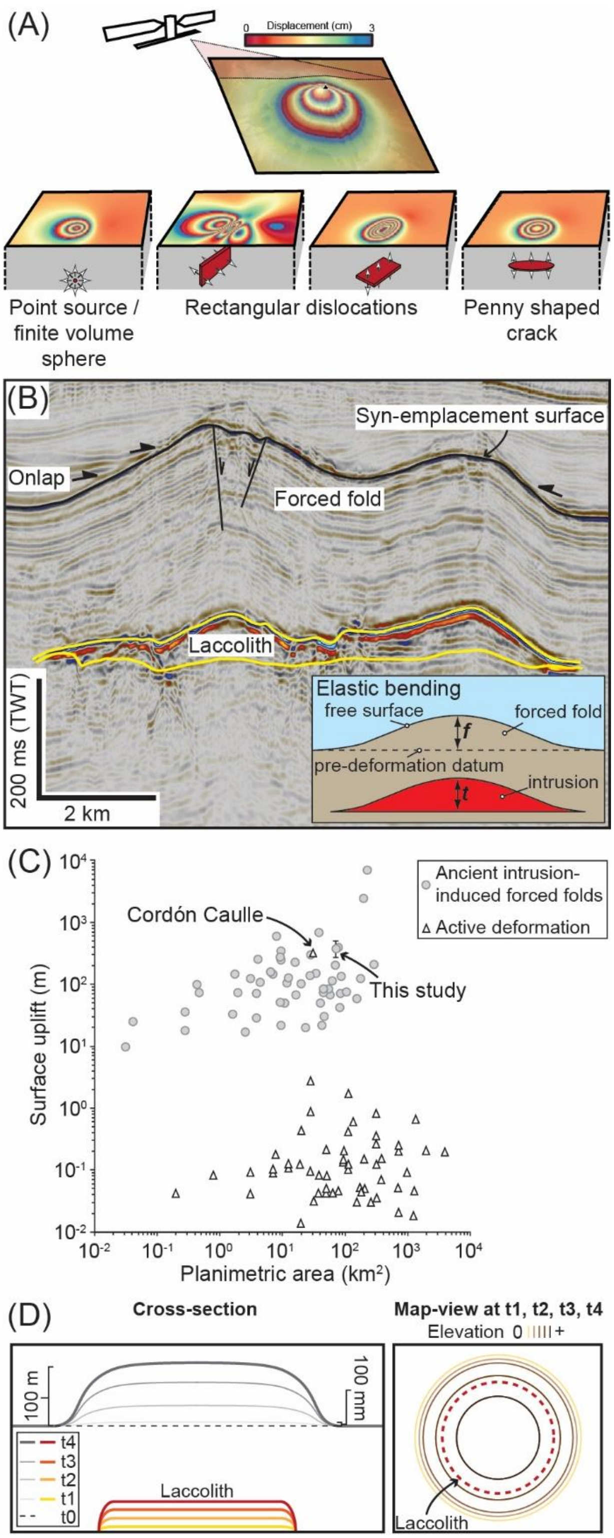

***Figure 1**: (A) Schematic showing how satellite-based Interferometric Synthetic Aperture Radar (InSAR) data can be used to monitor ground movements at volcanoes, and the expected surface displacement patterns predicted by different source geometries embedded in a homogeneous and isotropic elastic half-space (modified from Magee et al., 2018). (B)*

Time-migrated seismic reflection image from the Bight Basin, offshore S Australia, showing a buried laccolith and forced fold pair (modified from Jackson et al., 2013). Onlap of overlying reflections onto the forced fold denote its top, i.e., the syn-emplacement free surface. Vertical axis is in milliseconds two-way time (ms TWT). Inset: schematic showing fold amplitude (f) (i.e., uplift from the pre-deformation datum) and intrusion thickness (t) are expected to be similar if space for magma was solely generated by elastic bending (Pollard and Johnson, 1973; Galland and Scheibert, 2013). (C) Plot of intrusion-induced surface uplift measured from ancient forced folds, both observed in the field and seismic reflection data, and recorded by InSAR data at active volcanoes (see Supplementary Table 1 for data and references). (D) Sketch showing how laccolith and forced fold growth may relate through time.

Many volcano deformation models use analytical approaches that embed simple source geometries within homogeneous, isotropic, and linearly elastic host materials (Fig. 1A) (e.g., Mogi, 1958; Okada, 1985; McTigue, 1987; Fialko et al., 2001; Masterlark, 2007; Galland and Scheibert, 2013; Nikkhoo et al., 2016; Crozier et al., 2023). Of these models, most adopt an elastic half-space framework with a uniform pressure or volume change boundary condition applied to the source, which induces displacement around the entirety of the source (i.e. roof, floor, and side-wall deformation; e.g., Fig. 1A) (e.g., Mogi, 1958; Okada, 1985; McTigue, 1987; Fialko et al., 2001; Masterlark, 2007; Hautmann et al., 2010; Hickey et al., 2013). However, elastic half-space solutions may not be suitable for modelling shallow ($\lesssim$5 km) intrusions, where roof uplift via elastic bending dominates and little or no floor subsidence occurs (e.g., Jackson et al., 2013; van Wyk de Vries et al., 2014; Magee et al., 2019). For such shallow-level, tabular intrusions, some analytical methods apply thin elastic plate bending solutions to simulate displacement (Fig. 1B) (e.g., Pollard and Johnson, 1973; Kerr and Pollard, 1998; Bunger and Cruden, 2011; Galland and Scheibert, 2013; Castro et al., 2016; Scheibert et al., 2017). Regardless of whether simple analytical models use an elastic half-space or thin plate bending, we know they are wrong to some extent because: (1) assumptions of homogeneity and isotropy in the crust are rarely valid (e.g., Manconi et al., 2007; Segall, 2010; Galland, 2012; Hickey et al., 2016); and (2) they do not account for synchronous inelastic space-making processes (e.g., compaction, fluidisation) (e.g., Morgan et al., 2008; Currenti et al., 2010; Schofield et al., 2012). Yet simple analytical models remain widely used because uncertainties in their assumptions (and outputs) are outweighed by their low computational cost, which enable a first-order assessment of source properties in a timeframe pertinent to real-time decision-making during unrest (e.g., Garthwaite et al., 2019; Taylor et al., 2021; Parks et al., 2023). Furthermore, where little is known about the physical properties of the intrusion or surrounding crust, the simplifying assumptions of an elastic half space model may be preferable to poorly constrained complexity. Whilst simple analytical models do commonly fit observed displacement data, we expect there to be limits to their applicability (e.g., Battaglia and Hill, 2009; Crozier et al., 2023). Independent geophysical data (e.g., gravity), or testing sensitivity using synthetic data or analogue models (e.g., Crozier et al., 2023; Poppe et al., 2024), can provide insight into the suitability of an elastic half space or flexure-based approach. However, natural examples where known *and* modelled source properties can be confidently compared are very rare.

Seismic reflection data allow us to measure ancient, intrusion-induced surface uplift (forced folds) *and* determine the 3D geometry and location of underlying, solidified magma bodies at metre- to decametre-scale resolutions (Fig. 1B) (e.g., Hansen and Cartwright, 2006; Jackson et al., 2013; Magee et al., 2013; Reynolds et al., 2017). Here, we examine an Early Cretaceous laccolith that was emplaced at <2 km depth and uplifted (bended) overlying strata by 100's m across an area of ~14 km^2 in the Exmouth Plateau sedimentary basin, offshore

NW Australia (Dobb et al., 2022). We remove the effect of burial-related compaction to recover the final, pre-burial surface displacement developed over the lifetime of the laccolith (e.g., Smallwood, 2009; Magee et al., 2019). From these decompacted data we calculate syn-emplacement surface elevation changes and use these to extract plausible horizontal components of displacement, which we scale to mm–m based on the assumption of a uniform deformation rate. We aim to test whether our inferred surface displacements are well described by analytical volcano deformation models. Given the laccolithic geometry and shallow emplacement depth of the intrusion, we test the applicability of a thin plate bending solution (Galland and Scheibert, 2013) and penny shaped crack and rectangular dislocation elastic half-space models (e.g., Fig. 1A) (e.g., Okada, 1985; Fialko et al., 2001). We show that both analytical approaches, using either thin plate bending or elastic half-space methods, seem to reliably capture intrusion positions and lateral extents, but not emplacement depths. By analytically modelling surface displacement patterns extracted from seismic reflection data, we can compare estimated source properties to the observed parameters of natural intrusions in 3D.

2. Comparing geodetic and seismic reflection data

2.1 Seismic reflection data, intrusions, and forced folds

Seismic reflection data can image igneous intrusions, typically in sedimentary basins, and show that some are overlain by uplifted strata with current reliefs of 10's–100's m (Figs 1B and C) (e.g., Hansen and Cartwright, 2006; Jackson et al., 2013; Magee et al., 2019). We term these areas of overburden uplift 'forced folds' because their "*shape and trend are dominated by the shape of some forcing member* [i.e., a magma intrusion] *below*" (Stearns, 1978); by this definition, magmatic deformation at active volcanoes can also be categorized as forced folding (e.g., van Wyk de Vries et al., 2014; Karlstrom et al., 2018). Where such forced folds are imaged in seismic reflection data, or exposed at Earth's surface, they typically reveal the total lifetime impact of shallow-level (<4 km depths) intrusions on host rock deformation (Fig. 1B). Specifically, these examples show space is primarily generated by overburden uplift, often involving elastic bending (folding) and occasional faulting, with minimal or no floor subsidence (Fig. 1B) (e.g., Hansen and Cartwright, 2006; Magee et al., 2013; Magee et al., 2017a; Magee et al., 2018). Critically, the tops of intrusion-induced forced folds are often marked by onlap of overlying reflections, which indicates they represent the syn-emplacement free surface (Fig. 1B) (e.g., Trude et al., 2003; Hansen and Cartwright, 2006; Jackson et al., 2013). By removing the effects of burial-related compaction we can thus recover and quantify the final, pre-burial geometry of forced fold tops (Magee et al., 2019; Tian et al., 2021; Wang et al., 2022); i.e., from this we can measure the total intrusion-induced displacement of the surface.

2.2 Displacement scale

There are differences in the magnitude and timeframe of displacements estimated from seismic reflection data and from contemporary geodetic observations (e.g., GNSS, InSAR, or levelling) (Fig. 1C; Supplementary Table 1) (cf. Karlstrom et al., 2018). The geometry of seismically imaged forced folds captures the total surface displacement, typically 10's–100's m, acquired over the entire or most of the lifetime of shallow-level intrusions (Fig. 1C) (e.g., Magee et al., 2019; Tian et al., 2021; Wang et al., 2022). Yet it is often difficult to determine whether displacement accrued in a single intrusion event, or incrementally through multiple episodes of injection (e.g., Magee et al., 2017b; Reeves et al., 2018). In contrast, surface uplift at active volcanoes typically involves mm–m displacements recorded over days-to-years, reflecting only incremental recharge or growth of a magmatic system, and may be transient/reversible (at depths of ~0–15 km; Fig. 1C) (e.g., Menand, 2008; Ebmeier et al., 2018; Karlstrom et al., 2018; Biggs and Wright, 2020). Larger magnitudes of uplift akin to those observed in seismic reflection data have occasionally been observed at active volcanoes (e.g., Castro et al., 2016; Chadwick Jr et al., 2019). For example, 200 m of surface uplift across ~12 km^2 occurred over a month due to laccolith intrusion at Cordón Caulle, Chile in 2011 (Fig. 1C) (Castro et al., 2016).

Our seismic reflection data do not allow us to establish whether measured surface displacements accrued in a single event, or incrementally due to successive emplacement of small magma pulses. We explore a snapshot of forced fold development by scaling displacement magnitudes whilst maintaining their spatial pattern on the assumption that the laccolith grew incrementally due to a sequence of similar intrusions; i.e., this makes them similar in scale (i.e. mm–m) to surface movements often recorded at active volcanoes (Figs 1C and D). This snapshot of displacement could represent: (1) a portion of forced fold growth during one continuous intrusion event; or (2) a small-scale uplift event related to injection of a discrete magma pulse that contributed to incremental laccolith growth. Inherent to our approach is the assumption that laccolith and forced fold lateral dimensions were established early, with intrusion inflation and vertical uplift dominating after (Fig. 1D). This approach is motivated by the dimensional similarity of many ancient plutons, as well as overlap in planimetric areas of geodetically and seismically imaged displacement patterns (Fig. 1C) (e.g., Cruden and McCaffrey, 2001; Karlstrom et al., 2018). These geometrical similarities suggest intrusion growth occurs via horizontal expansion before thickening (e.g., Cruden and McCaffrey, 2001; Menand, 2008).

2.3 3D displacement distribution

Many elastic half-space models assume magma reservoir recharge or growth results in roof uplift and floor subsidence, as well as side-wall displacement in some solutions (e.g., Fig.

1A) (e.g., Mogi, 1958; Okada, 1985; McTigue, 1987; Fialko et al., 2001). Yet seismic reflection data, as well as field observations, reveal displacement associated with shallow-level intrusions is often accommodated by roof uplift via elastic bending (Fig. 1B) (e.g., Pollard and Johnson, 1973; Koch et al., 1981; Magee et al., 2013). Where roof uplift via elastic bending is the only mechanism creating space for magma, we may expect the amplitude and volume of the forced fold relates simply to the intrusion thickness and volume, depending on its depth and pressure (Pollard and Johnson, 1973; Bunger and Cruden, 2011; Galland and Scheibert, 2013; Scheibert et al., 2017). However, if we were to invert surface displacements from uplift generated by elastic bending using elastic half-space models, our estimated source properties would be based on the assumption that floor subsidence, and potentially side-wall deformation depending on model chosen, contributes to space generation (Fig. 1A). In this scenario, we would expect a rectangular dislocation or penny-shaped crack analytical solution to overestimate source depth and volume change.

3. Seismic reflection analysis

In this section we: (1) provide the geological context of our study area; (2) describe the seismic reflection data and our decompaction method; and (3) present the decompacted surface displacement pattern of the forced fold.

3.1 Geological setting

The Exmouth Plateau covers ~300,000 km^2 of the North Carnarvon Basin, offshore NW Australia (Fig. 2A) (e.g., Willcox and Exon, 1976; Longley et al., 2002; Stagg et al., 2004; Direen et al., 2008). As Australia and Greater India separated in the Mesozoic, rifting produced normal faults that: (1) offset the Triassic, fluvio-deltaic, siliciclastic Mungaroo Formation; and (2) accommodated a thin siliciclastic sequence of Late Triassic-to-Jurassic shallow marine sandstones and siltstones (e.g., Brigadier Formation and Murat Siltstone) and the deep marine Dingo Claystone (Figs 2A-C) (e.g., Willcox and Exon, 1976; Tindale et al., 1998; Stagg et al., 2004; Bilal and McClay, 2022). Regional uplift and development of the Base Cretaceous unconformity towards the end of rifting preceded rapid subsidence and deposition of the Barrow Group (e.g., Reeve et al., 2016; Paumard et al., 2018; Reeve et al., 2022). Magmatism between the Kimmeridgian and Berriasian produced sills and dykes within these strata across the southern extent of the North Carnarvon Basin (e.g., Fig. 2C) (e.g., Symonds et al., 1998; Magee et al., 2013; Rohrman, 2013; Magee et al., 2017b; Magee and Jackson, 2020; Norcliffe et al., 2021; Curtis et al., 2023).

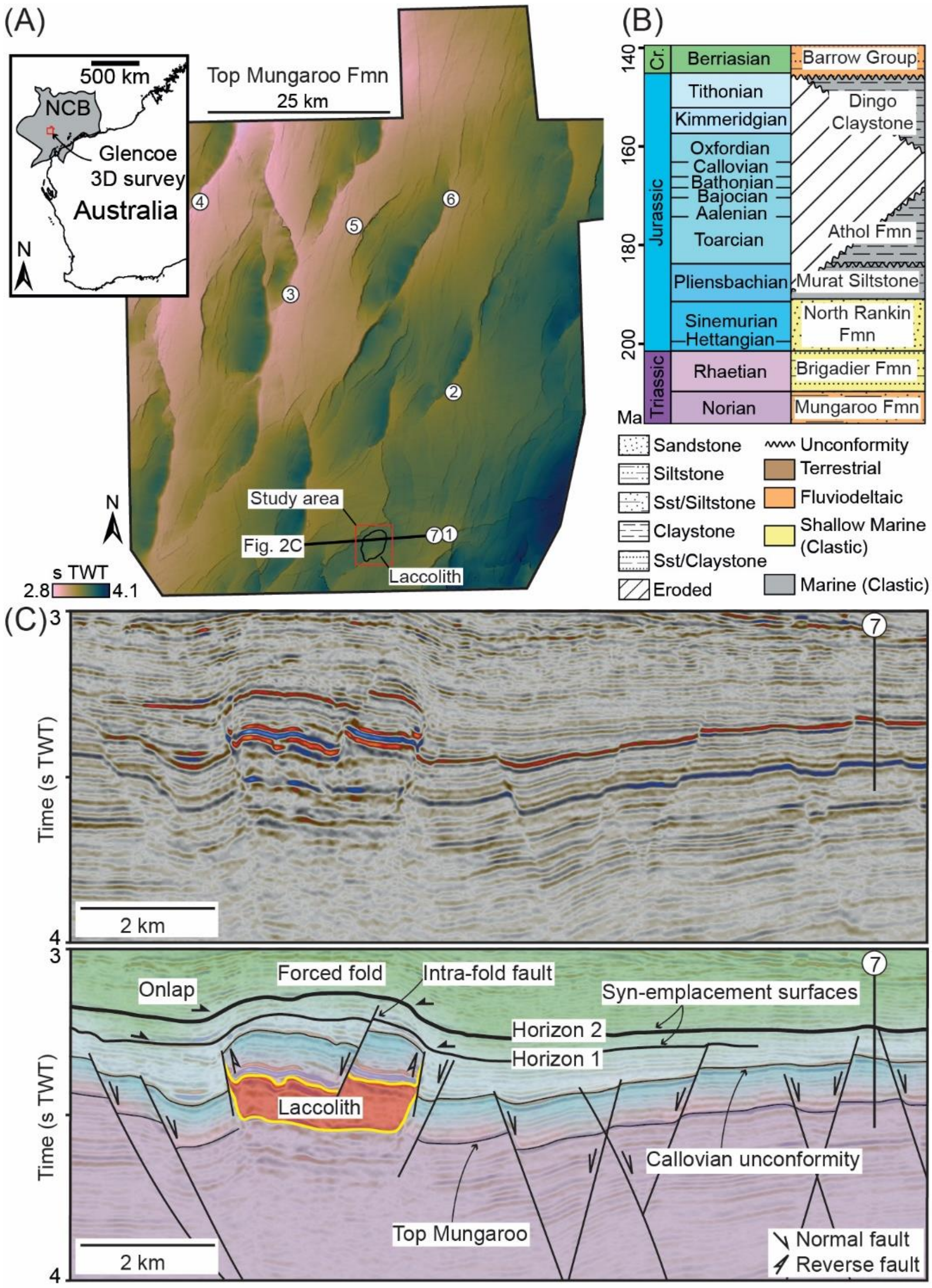

***Figure 2**: (A) Time-structure map of the Top Mungaroo Formation highlighting the normal fault architecture across the Glencoe 3D survey, as well as the study area and outline of the laccolith (Dobb et al., 2022). Borehole locations shown are: 1 = Chester-1ST1; 2 = Warror-1; 3 = Nimblefoot-1; 4 = Rimfire-1; 5 = Glencoe-1; 6 = Briseis-1; 7 = Chester-2. Inset: location of the Glencoe 3D survey within the North Carnarvon Basin (NCB) offshore NW Australia. (B) Stratigraphic column for the study area (based on Hocking et al., 1987; Hocking, 1992; Tindale et al., 1998; Longley et al., 2002). (C) Uninterpreted and interpreted*

seismic reflection sections showing the structural and stratigraphic framework for the laccolith and forced fold stratigraphic framework of the studied intrusion and fold (modified from Dobb et al., 2022). See Figure 2A for location.

The laccolith we study is ~4.5 × 3.0 km in plan-view and comprises a main tabular body typically ~260–320 m thick, but up to 504–617 m thick in places, and encompassing inclined sheets up to ~300 m high (Fig. 2C) (Dobb et al., 2022). Seismic-stratigraphic onlap relationships onto the overlying forced fold indicate it, and the laccolith, likely formed in the Berriasian during two principal phases of activity (Fig. 2C) (Dobb et al., 2022; Curtis et al., 2023); we cannot decipher whether each of these two phases of activity represent single events, or if they comprised multiple, incremental intrusion and deformation episodes. The first phase of laccolith and forced fold development occurred when Horizon 1 marked the contemporaneous free surface (Fig. 2C). The top of the forced fold, Horizon 2, marks the second phase of laccolith emplacement and here the fold is ~5.0 × 3.5 km in plan-view, has a subtle dome-shaped morphology with a monoclinal rim, and has a current maximum amplitude (f_{max}) of ~191–268 m (Fig. 2C) (Dobb et al., 2022). Development of reverse faults above the edges of the laccolith and outer-arc extensional (intra-fold) faults across the fold accompanied uplift (Figs 2C) (Dobb et al., 2022; Curtis et al., 2023). There is no evidence for post-emplacement modification of or erosion across the forced fold (Dobb et al., 2022). Minor folding of strata occurs above Horizon 2 but this deformation is attributable to differential compaction during burial (Fig. 2C) (Dobb et al., 2022).

3.2 Data

The Glencoe 3D seismic reflection survey is zero-phase and time-migrated, covering an area of ~4042 km^2 with a line spacing of 25 m and recorded to a depth of ~8 s two-way time

(TWT) (Fig. 2A). Although no boreholes intersect the forced fold, we use boreholes across the Glencoe survey to (Fig. 2C) (Harmer and Whelan, 2012): (1) determine the lithology of the folded strata; (2) establish a time-depth relationship for the sedimentary sequence, allowing us to depth-convert measurements from seconds two-way time (TWT) to metres (Supplementary Figure 1 and Supplementary Table 2); and (3) calculate the limits of separability and visibility (i.e., indicators of vertical resolution), which given a dominant frequency of 25 Hz are ~56 (±6) m and ~7 (±1) m, respectively (Dobb et al., 2022). The horizontal resolution of the time-migrated seismic reflection data is likely up to ~30 (±5) m (i.e., λ/4). We depth-convert laccolith measurements assuming the intrusion has a seismic velocity of ~5.55(±10%) km s^{-1}, which captures the typical range of mafic igneous rocks (e.g., Skogly, 1998; Planke et al., 2005; Magee et al., 2015).

3.3 Decompaction method

As ancient intrusions and forced folds are buried within sedimentary basins, compaction of the folded strata reduces the fold amplitude and the vertical distance between the fold and intrusion tops (i.e., emplacement depth) (e.g., Magee et al., 2019). We focus solely on the second phase of laccolith development and its corresponding displacement of Horizon 2. To remove the effects of burial-related compaction and recover the initial forced fold geometry at Horizon 2 (i.e., its surface displacement pattern), we decompact and backstrip the folded sequence (Magee et al., 2019). We first define a likely pre-deformation datum for Horizon 2 by removing the fold and extrapolating the regional trend of the remaining surface across this cropped area (e.g., Fig. 3A). From both Horizon 2 and its pre-deformation datum, as well the top and base laccolith surfaces, we extract gridded point arrays with regular 50 m spacings. The points comprising each array have coincident x and y co-ordinates and thus just vary in their depth (z) (Fig. 3A). We denote Horizon 2 depths as $z1$, with depths of its pre-deformation datum being $z2_a$; the current fold amplitude (f) at Horizon 2 is thus $z1 - z2_a$ (Figs 3A and B).

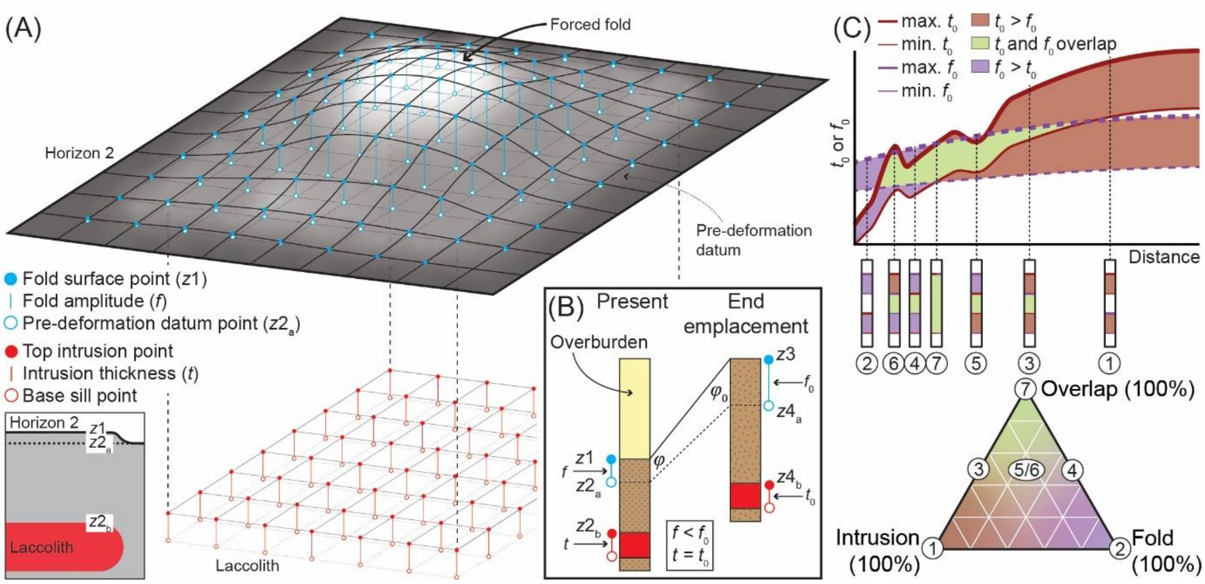

Figure 3A*: (A) Schematic showing how the top forced fold surface, its pre-deformation datum, and the top and base laccolith contacts are gridded into point arrays. (B) Sketch of decompaction process involving removal of the overburden and recovery of initial porosity (φ_0), such that z1 becomes z3 and the initial fold amplitude (f_0) and laccolith emplacement depth can be calculated by converting $z2_a$ and $z2_b$ to $z4_a$ and $z4_b$, respectively (based on Allen and Allen, 2013). (C) Plots showing possible relationships between the error envelopes for the initial fold amplitude (f_0) and intrusion thickness (t_0) given conservative maximum (max.) and minimum (min.) estimates for both. There are seven possible scenarios: (1) $t_0 > f_0$; (2) $t_0 < f_0$; (3) $t_0 > f_0$ but there is some overlap where we cannot know whether t_0 or f_0 is greater for that restricted parameter range; (4) $t_0 < f_0$ but there is some overlap; (5 and 6) either $t_0 > f_0$, $t_0 < f_0$, or they overlap; and (7) the error envelopes of both t_0 and f_0 completely overlap. Scenarios 1, 2, and 7 represent end-members that can be assigned to the corners of a ternary diagram, whereas scenarios 3 and 4 will lie somewhere on the intrusion-overlap or fold-overlap axis, respectively. Scenarios 5 and 6 will plot in the interior of the ternary diagram.*

We remove the overburden, such that $z1$ becomes the new free surface ($z3$ = 0 m), and restore the current porosity (φ) of the folded sequence to its initial porosity (φ_0) using:

$$z4 - z3 = z2 - z1 - \frac{\varphi_0}{c}(e^{-cz1} - e^{-cz2}) + \frac{\varphi_0}{c}(e^{-cz3} - e^{-cz4}) \quad (1)$$

where c is the compaction coefficient (Fig. 3B) (Allen and Allen, 2013). With equation 1 we convert $z2$ to $z4$, such that the initial fold amplitude (f_0) of Horizon 2 is $z3$ - $z4$ (Figs 3A and B). Treating the laccolith top as $z2_b$ (and thus $z4_b$) also allows us to estimate laccolith emplacement depths (Magee et al., 2019). We consider that once solidified and cooled, the laccolith was incompressible, so its current thickness (t) is equivalent to its initial thickness (t_0) (Fig. 3B).

Our decompaction approach is limited because estimates of φ_0 and c are not available for the folded strata analysed (Dobb et al., 2022). To account for this uncertainty, we use a range of realistic values for of φ_0 and c given that the Chester-2 borehole indicates the folded sequence comprises interbedded sandstones, siltstones, marls, and calcilutites (Harmer and Whelan, 2012). Specifically, we consider φ_0 ranges from 0.2–0.68, consistent with a range of siliciclastic sequences, and c ranges from 0.1–0.7 km (Allen and Allen, 2013; Lai et al., 2022). To compare t_0 and f_0 given our uncertainty in their input variables (e.g., seismic velocities and material properties), we calculate percentage probabilities and use a ternary plot to define where t_0 or f_0 may be greater, or if their range overlaps, at any given point (Fig. 3C). As the end-members of our input parameter ranges are extreme and represent less likely scenarios, we also provide decompacted measurements considering a probable scenario where the folded succession is a muddy sandstone, consistent with local borehole data, with a

φ_0 of 0.55 and c of 0.39 (Allen and Allen, 2013), and the seismic velocity of the laccolith is 5.55 km s^{-1}. All data are provided in Supplementary Table 3.

3.4 Results

The elevation change pattern of the forced fold is broadly dome-shaped at Horizon 2 with prominent monoclinal rims (Figs 2C and 4A). Our decompaction analysis reveals that the fold here covers an area of ~17 km^2, had an initial maximum amplitude ($f_{0\max}$) of ~189–402 m, and a volume of ~1.1–2.6 km^3 (Figs 1C and 4B). For our probable scenario, $f_{0\max}$ is ~309 m and the fold volume ~1.9 km^3 (Fig. 4B). In comparison, the laccolith has an area of ~10 km^2, an initial maximum thickness ($t_{0\max}$) of ~509–662 m, and volume of ~2.7–3.3 km^3 (Fig. 4B). Regardless of uncertainty in variables used in our decompaction analysis, the laccolith seems consistently thicker than or at least broadly similar to f_0, except around its edge and partly along a NNE-trending linear zone that extends northwards from the intrusion centre (Fig. 4C). The mean depth of the top laccolith beneath Horizon 2 ranges from ~0.50–0.89 km and is ~0.76 km for the considered probable scenario; the decompacted, syn-emplacement centroid depth range of the laccolith is ~0.63–1.05 km given it is on average ~260–320 m thick (Fig. 4C). For a mean laccolith length of ~3.75 km, the radius-to-depth ratio of the laccolith is thus ~3.6–6.0.

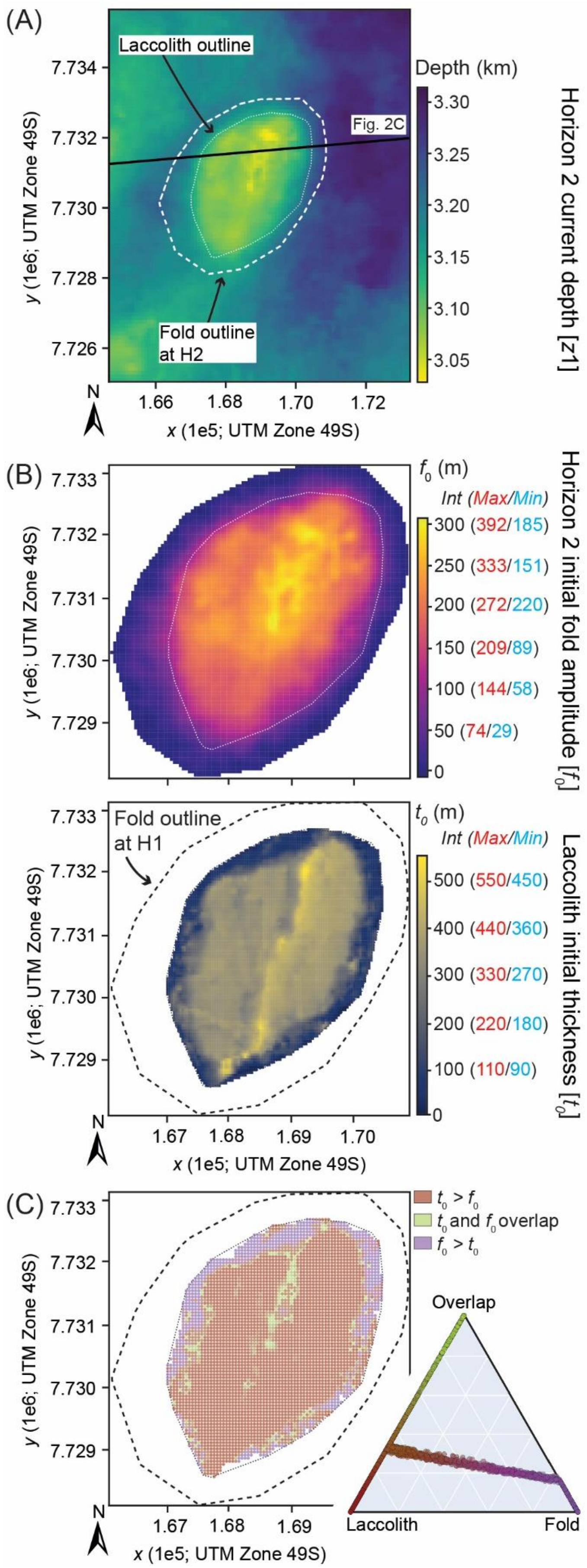

(A)
Laccolith outline
Fold outline at H2
Fig. 2C
Depth (km)
Horizon 2 current depth [z1]
y (1e6; UTM Zone 49S)
x (1e5; UTM Zone 49S)
N
(B)
f_0 (m)
Int (Max/Min)
300 (392/185)
250 (333/151)
200 (272/220)
150 (209/89)
100 (144/58)
50 (74/29)
Horizon 2 initial fold amplitude [f_0]
Fold outline at H1
t_0 (m)
Int (Max/Min)
500 (550/450)
400 (440/360)
300 (330/270)
200 (220/180)
100 (110/90)
Laccolith initial thickness [t_0]
(C)
$t_0 > f_0$
t_0 and f_0 overlap
$f_0 > t_0$
Overlap
Laccolith
Fold

359

***Figure 4**: (A) Depth-converted structure map of Horizon 2 within the study area. (B) Initial fold amplitude and laccolith thickness maps following decompaction and backstripping of the overburden. Because we cannot know the initial porosity (φ_0) or compaction coefficient (c) of the deformed strata we calculate maximum (Max) and minimum (Min) end-members, and a probable intermediate (Int) scenario. Similarly, for the laccolith, we do not know its seismic velocity, so we calculate maximum (Max) and minimum (Min) end-members, and a probable intermediate (Int) scenario, assuming its velocity is 5.55(±10%) km s^{-1}. (C) Map and ternary diagram depicting likely relationships between initial fold amplitude and laccolith thickness given uncertainties in input parameters.*

4. Analysing ancient deformation

We have decompacted the surface displacement of the forced fold at Horizon 2 and quantified the underlying laccolith geometry, whilst accounting for uncertainties in our analysis. Here, we describe the modelling approach employed to estimate potential source properties from this surface displacement data. We recognise that some emplacement and folding occurred prior to deposition of Horizon 2 (Fig. 2C), when Horizon 1 marked the contemporaneous surface (Dobb et al., 2022). The surface displacements we recover from decompaction of Horizon 2 will therefore not wholly reflect the full geometry (volume or thickness) of the laccolith. However, we still expect estimated source location, plan-view size (e.g., radius), and emplacement depths to broadly equal those of the observed laccolith. Given the tabular geometry of the intrusion studied (e.g., Fig. 2C), we test analytical solutions for bending of a thin elastic plate above shallow-level laccoliths (Galland and Scheibert, 2013) and displacements around penny-shaped crack and rectangular dislocation sources embedded within an elastic half-space (Okada, 1985; Fialko et al., 2001).

4.1 From elevation change to co-intrusive displacements

Volcano deformation modelling aims to estimate source intrusion properties from measured surface displacements (e.g., Segall, 2010). By decompacting our seismic reflection data, we recover the distribution of surface displacement for the forced fold (i.e., its initial geometry) and from this measure the initial fold amplitude (f_0) (Fig. 4B). These f_0 measurements describe the elevation change, i.e., vertical displacement (U_Z), at any location across the forced fold (Fig. 5A). To align these surface displacement measurements with data we may collect at active volcanoes, we create a triangular mesh from our Horizon 2 point-array and for each resolved triangle define the x and y co-ordinates of their centroid and a corresponding mean U_Z of its three vertices (Figs 3A and 5A). We can consider each of these centroids as equivalent to a levelling station; i.e., instruments that solely record changes in elevation (e.g., Fig. 5B) (e.g., Sigmundsson et al., 2018). By inverting this U_Z data we can thus model an end-member scenario where all displacements have a vertical trajectory (Fig. 5B).

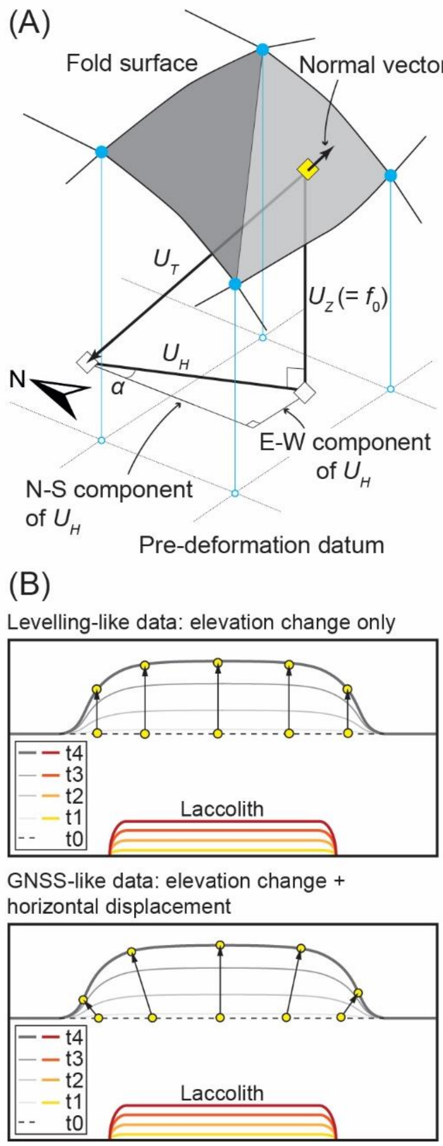

Figure 5*: (A) Sketch showing derivation of vertical (U_Z), horizontal (U_H), and total (U_T) displacement components for each centroid of a triangular mesh. (C) Schematic showing the difference in displacement trajectories between levelling stations, which only record vertical movements, and GNSS stations, which record the full 3D displacement field.*

Horizontal surface displacements (U_H) are sensitive to, and thus help constrain, source geometry (e.g., Battaglia and Hill, 2009). However, we cannot determine the occurrence or magnitude of U_H using seismic reflection data. We therefore simulate a plausible scenario by estimating horizontal displacements from our U_Z data and assuming the local pre-deformation datum followed the regional-trend topography of Horizon 2. Specifically, we project the mean normal vector of each triangle within the mesh from its centroid down to the pre-deformation datum (Fig. 5A). From these vectors we can trigonometrically determine a possible U_H and its north-south and east-west components (Fig. 5A). By using our measured U_Z data and estimating U_H, we can consider each centroid as equivalent to a GNSS station; i.e., instruments that record changes in elevation and lateral position (e.g., Fig. 5B) (e.g., Dzurisin, 2006). Implicit to our scenario involving U_H derived from the fold surface normal is that displacement occurred along radial trajectories (Fig. 5B).

Our calculated U_Z and U_H displacements represent the total surface movement associated with cumulative laccolith emplacement. However, the magnitudes of our displacements are 10's–100's m, unlike the mm–m scale deformation we observe at many active volcanoes (Fig. 1D). To aid comparison between ancient and active systems, we scale our calculated displacement by 10^3, moving from m- to mm-scale deformation Fig. 1D). This mm-scale scenario likely does not reflect an actual stage of forced fold growth but we treat this as a theoretical scenario where the laccolith was built up gradual by successive, similar intrusions (e.g., Figs 1D and 5B). Our mm-scale scenario maintains the relative fold geometry, so we expect estimated source locations and emplacement depths to be broadly commensurate with measurements.

4.2 Modelling procedure

4.2.1 Thin plate bending

Thin elastic plate theory describes how the flexural rigidity of a material, i.e., its resistance to bending, effects the displacement of a plate as a transverse load is applied (Fig. 1B) (e.g., Timoshenko and Woinowsky-Krieger, 1959). We use an axisymmetric, analytical, forward model to formulate surface displacements generated by bending of a thin elastic plate above a tabular intrusion lying on a deformable elastic foundation (Galland and Scheibert, 2013). As the observed forced fold extends beyond the laterals limits of the laccolith (Figs 2C and 4A), we expect the elastic foundation (underburden) to be softer than the overlying bending plate (Galland and Scheibert, 2013). We compare these predicted vertical and horizontal displacement profiles to those measured along a transect that extends from the centre of the laccolith to the NE along its long axis. For each modelled displacement profile, we characterise its fit to our measured displacement data through R^2 and mean percentage error analyses (e.g., Castro et al., 2016). Within our models we assign Poisson's ratio (v) to equal 0.25, as is often assumed in the volcano deformation literature (see Heap et al., 2020 and references therein). Due to uncertainties in other input variables, we model a range of scenarios, constrained where possible by our data, and assume a uniform pressure distribution within the laccolith (Table 1). Other thin plate bending solutions that account for fracture propagation, magma flow, magma weight, and/or plastic host rock deformation at intrusion tips are available (e.g., Bunger and Cruden, 2011; Scheibert et al., 2017). We do not utilise these solutions currently because their additional variables and associated uncertainties add further complexity while we choose to focus on first-order similarities.

Table 1: Input parameters for thin plate elastic bending using the analytical solution of Galland and Scheibert (2013)

Variable description	Notation	Unit	Values	Justification
Laccolith radius	*a*	m	3000, 4500	Measured laccolith short and long axes
Laccolith depth	*h*	m	500, 890	Decompacted emplacement depth estimates of top laccolith
Young's modulus	*E*	Pa	0.01e10, 0.1e10, 1e10, 2e10	0.1-20 GPa considered reasonable for weakly lithified seafloor muddy sandstones
Pressure distribution parameter	*n*	-	0	Uniform pressure distribution
Elastic foundation stiffness	*k*	N/m^3	10e5, 10e7	Poorly constrained but found reasonable by Castro et al., (2016)
Pressure at laccolith centre and periphery	*P* and *Pa*	Pa	1e2, 1e3	Other values tried but these produced best fits. *P* and *Pa* equal to maintain uniform pressure

4.2.2 Elastic half-space modelling

For our elastic half-space analytical modelling, we invert surface displacements using Geodetic Bayesian Inversion Software (GBIS) and Volcano Source Modelling (VSM) software to estimate geodetic source (intrusion) properties (Bagnardi and Hooper, 2018; Trasatti, 2022). We specifically use GBIS to model the proxy GNSS data as it is a more widely used software, and VSM for modelling the levelling stations as it has built-in functionality to handle these data (Bagnardi and Hooper, 2018; Trasatti, 2022). For computational efficiency of the elastic half-space solutions, we randomly downsample the number of modelled triangle centroids (stations) from 13,765 to 25 (Supplementary Tables 4 and 5). To account for uncertainty in the data, we randomly assign a standard deviation error of 1–10 mm to the displacement components for each station (Supplementary Tables 4 and 5), which is consistent with typical error magnitudes (Bagnardi and Hooper, 2018). Within our models we assign Poisson's ratio (v) to equal 0.25, as is often assumed in the volcano deformation literature (see Heap et al., 2020 and references therein), and where relevant we arbitrarily set Young's modulus (E) to 1 GPa. In VSM we use both the Bayesian inversion (BI) and neighbourhood algorithm (NA) approaches for inverse modelling (Trasatti, 2022). For each GBIS and VSM model, regardless of the inversion method, we test 1×10^6 samples (Bagnardi and Hooper, 2018; Trasatti, 2022).

As a first-pass assessment of model validity, we present either: (1) the 2.5 and 97.5 percentiles of each intrusion variable calculated by GBIS (Bagnardi and Hooper, 2018); or (2) the misfit calculated in VSM (Trasatti, 2022). From the optimal source properties defined for each inverse model, we forward model the intrusion parameters to generate predicted displacements across the entire forced fold (Bagnardi and Hooper, 2018). We then compare these predicted displacements to those of our depth-converted and decompacted fold measurements by calculating residuals (Bagnardi and Hooper, 2018). Although our displacement data are normalised to mm-scales, we calculate the mean percentage error of these residuals at the 25 stations used in our inverse models as a relative proxy for quality of fit.

4.3 Modelling results

4.3.1 Thin plate bending

Our thin plate elastic bending models all predict vertical displacements that have a bell-shaped morphology, peaking above the laccolith centroid (e.g., Fig. 6; Supplementary File 1). Horizontal displacements reduce to 0 m above the laccolith centroid and peak towards its lateral edge (e.g., Fig. 6; Supplementary File 1). These modelled vertical and horizontal displacements all extend beyond the recognised limit of the forced fold, to greater distances for larger modelled laccoliths (e.g., Fig. 6). Many input parameter combinations modelled produce extremely poor fits to measured displacements, particularly for horizontal displacements (Table 2). However, some modelled vertical displacement profiles display R^2 fits of >0.5 (up to 0.9) to measured vertical displacements, although their corresponding mean percentage errors are still >100% (Table 2). These quality-of-fit indices suggest that thin-plate bending cannot easily describe the shape of the ancient displacements (Fig. 6; Table 2).

Figure 6

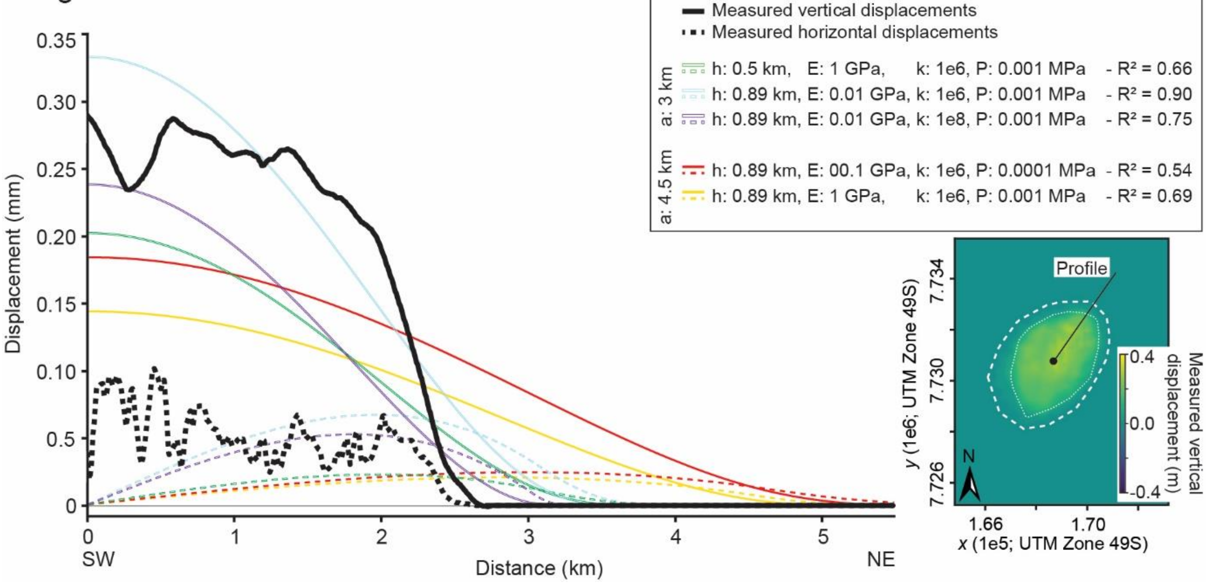

Figure 6*: Plot comparing measured vertical (U_Z) and horizontal (U_H) displacements to those modelled using a thin plate bending analytical solution (Galland and Scheibert, 2013). Only modelled input parameter combinations producing R^2 fits to the data >0.5 are plotted. The inset map highlights the plot profile extends from the fold centroid along its long axis to the NE.*

Table 2: Thin elastic plate bending modelling results

Input variable					R^2 value		Mean percentage error	
a (km)	*h* (km)	*E* (GPa)	*k* (N/m^3)	Overpressure* (MPa)	Vertical displ.	Horizontal displ.	Vertical displ. (%)	Horizontal displ. (%)
3.0	0.50	20.0	1.00E+08	0.0001	-1.34	-1.14	100	104
				0.001	-1.23	-1.10	106	202
			1.00E+06	0.0001	-1.32	-1.14	104	117
				0.001	-1.08	-1.08	159	343
		10.0	1.00E+08	0.0001	-1.33	-1.13	100	112
				0.001	-1.13	-1.06	111	295
			1.00E+06	0.0001	-1.30	-1.13	106	135
				0.001	-0.90	-1.02	187	534
		01.0	1.00E+08	0.0001	-1.16	-1.07	2	250
				0.001	0.17	-0.50	179	1747
			1.00E+06	0.0001	-1.06	-1.05	129	379
				0.001	0.66	-0.40	466	3073
		00.1	1.00E+08	0.0001	0.07	-0.52	147	1490
				0.001	-	-	1176	14527
			1.00E+06	0.0001	0.36	-0.46	257	2217
				0.001	-	-	2506	21875
	0.89	20.0	1.00E+08	0.0001	-1.35	-1.14	100	99
				0.001	-1.32	-1.13	102	137
			1.00E+06	0.0001	-1.34	-1.14	101	104
				0.001	-1.27	-1.12	122	205
		10.0	1.00E+08	0.0001	-1.35	-1.14	100	102
				0.001	-1.30	-1.11	103	173
			1.00E+06	0.0001	-1.34	-1.14	102	112
				0.001	-1.22	-1.09	133	288
		01.0	1.00E+08	0.0001	-1.31	-1.12	101	151
				0.001	-0.98	-0.90	118	707
			1.00E+06	0.0001	-1.28	-1.11	109	214
				0.001	-0.68	-0.81	222	1364
		00.1	1.00E+08	0.0001	-1.03	-0.92	108	580
				0.001	0.75	0.00	234	5132
			1.00E+06	0.0001	-0.89	-0.87	143	939
				0.001	0.90	-0.39	651	8764
4.5	0.50	20.0	1.00E+08	0.0001	-0.67	-0.63	116	141
				0.001	-0.29	-0.56	306	594
			1.00E+06	0.0001	-0.64	-0.62	138	161
				0.001	-0.03	-0.54	550	807
		10.0	1.00E+08	0.0001	-0.63	-0.62	134	187
				0.001	0.04	-0.49	502	1078
			1.00E+06	0.0001	-0.58	-0.61	168	221
				0.001	0.36	-0.46	885	1434
		01.0	1.00E+08	0.0001	-0.02	-0.49	445	1009
				0.001	-	-0.62	4002	9424
			1.00E+06	0.0001	0.15	-0.48	620	1204
				0.001	-	-1.27	5904	11390
		00.1	1.00E+08	0.0001	-	-0.53	3678	9039
				0.001	-	-	37636	90646
			1.00E+06	0.0001	-	-0.82	4628	10121
				0.001	-	-	47138	101522
	0.89	20.0	1.00E+08	0.0001	-0.71	-0.63	103	110
				0.001	-0.62	-0.61	139	263
			1.00E+06	0.0001	-0.70	-0.63	109	119
				0.001	-0.52	-0.59	221	366
		10.0	1.00E+08	0.0001	-0.70	-0.63	105	124
				0.001	-0.55	-0.58	176	423
			1.00E+06	0.0001	-0.68	-0.63	116	141
				0.001	-0.39	-0.56	302	599
		01.0	1.00E+08	0.0001	-0.57	-0.59	160	390
				0.001	0.43	-0.30	798	3171
			1.00E+06	0.0001	-0.50	-0.57	212	485
				0.001	0.69	-0.34	1357	4139
		00.1	1.00E+08	0.0001	0.36	-0.30	712	2982
				0.001	-	-	6992	29412
			1.00E+06	0.0001	0.54	-0.30	973	3513
				0.001	-	-	9811	34777

*Magma overpressure is calculated from input P and Pa values, and lithostatic load (see Galland and Scheibert, 2013)

4.3.2 Elastic half-space models

Most of our inverse models converge to a best-fit solution, except for models of levelling-like data (i.e., just U_Z) using the penny shaped crack solution in VSM, which does not converge for either the BI or NA methods (Supplementary Table 3; Supplementary File 2). The estimated intrusion centroids for all converging penny shaped crack and rectangular dislocation models are within 500 m of the measured laccolith horizontal location (Figs 7 and 8; Supplementary Table 6). Rectangular dislocation sources retrieved from analytical models have a similar strike and planimetric area (8.65–11.24 km^2) to the observed laccolith (~10 km^2), and there is little difference between those obtained from our simulated 3D displacements (Figs 7 and 8; Supplementary Table 6). The rectangular dislocation sources are shorter than the laccolith as defined by the seismic reflection data, but their corners extend beyond the laccolith limits (Figs 7 and 8). Measured vertical displacements are greater than those modelled, except above these rectangular source corners (Figs 7 and 8); i.e., the forced fold seen in the seismic reflection data has a dome-like morphology, but rectangular dislocation models would predict flat-topped deformation. Mean percentage errors for the measured and rectangular dislocation model vertical displacements are 28–42% (Supplementary Table 6). In contrast to the rectangular dislocation sources, the optimal penny-shaped crack source has a diameter similar to the laccolith long axis and forced fold short axis, and a planimetric area of 15.11 km^2 (Fig. 8; Supplementary Table 6). Vertical displacements modelled above the penny shaped crack source are greater than those measured above the laccolith centroid, but less than measured vertical displacements above the NE and SW portions of the laccolith (Fig. 8). The mean percentage error for the measured and penny shaped crack model vertical displacements is 57% (Supplementary Table 6). The estimated distribution of E-W and N-S horizontal displacement derived from our seismic reflection data is more complex than that predicted by the optimal models (Fig. 8). Although there are similarities in the pattern and magnitude of measured and modelled horizontal displacements, they have mean percentage errors >140% (Fig. 8; Supplementary Table 6). Estimated centroid (emplacement) depths for the penny shaped crack and rectangular dislocation models are 0.16–0.41 km (Supplementary Table 6), which do not overlap with the decompacted emplacement depth range of the laccolith centroid (~0.63–1.05 km).

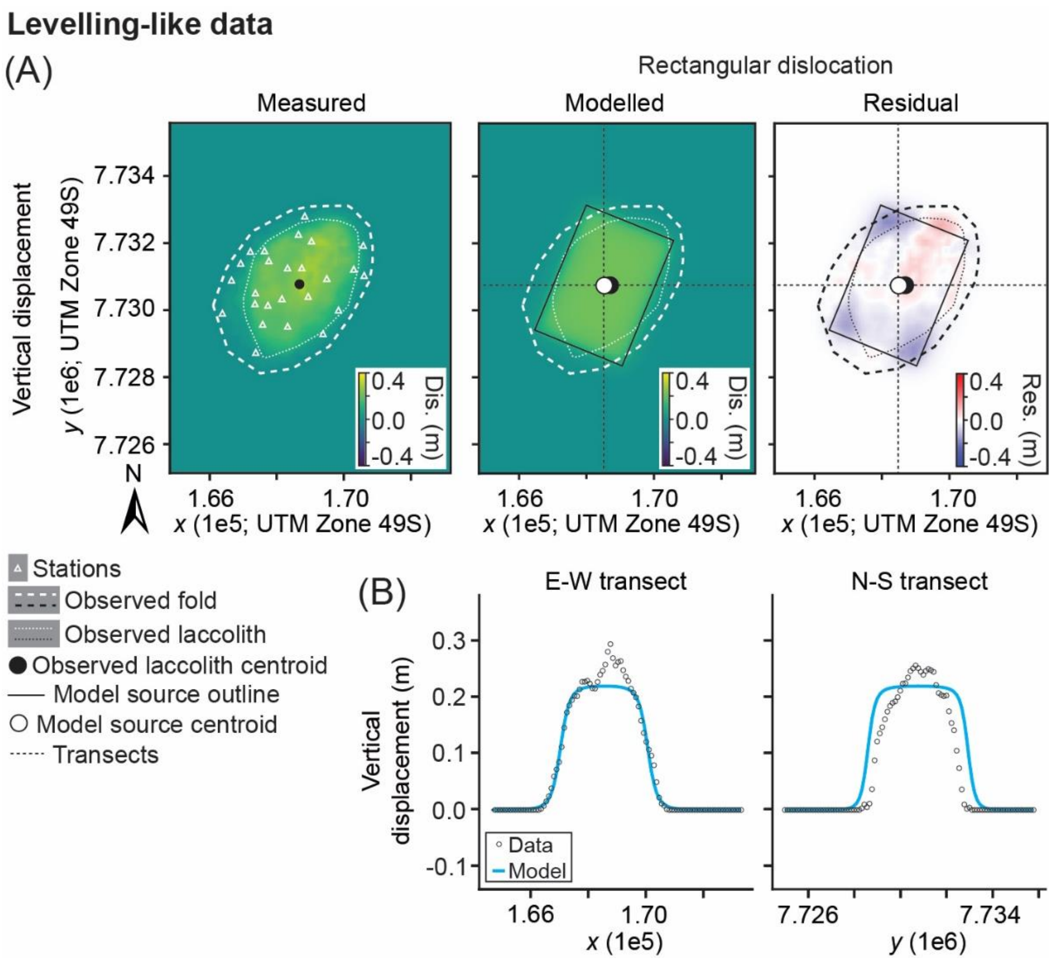

***Figure 7**: (A) Map of measured U_Z, highlighting the 25 stations selected for modelling, compared to a forward model of the optimal scenario derived from inverse modelling of levelling-like data. Residual map highlights the difference to measured displacement (displ.). (B) Transects oriented E-W and N-S through the area (see maps for locations) are also provided to compare measured and modelled displacement.*

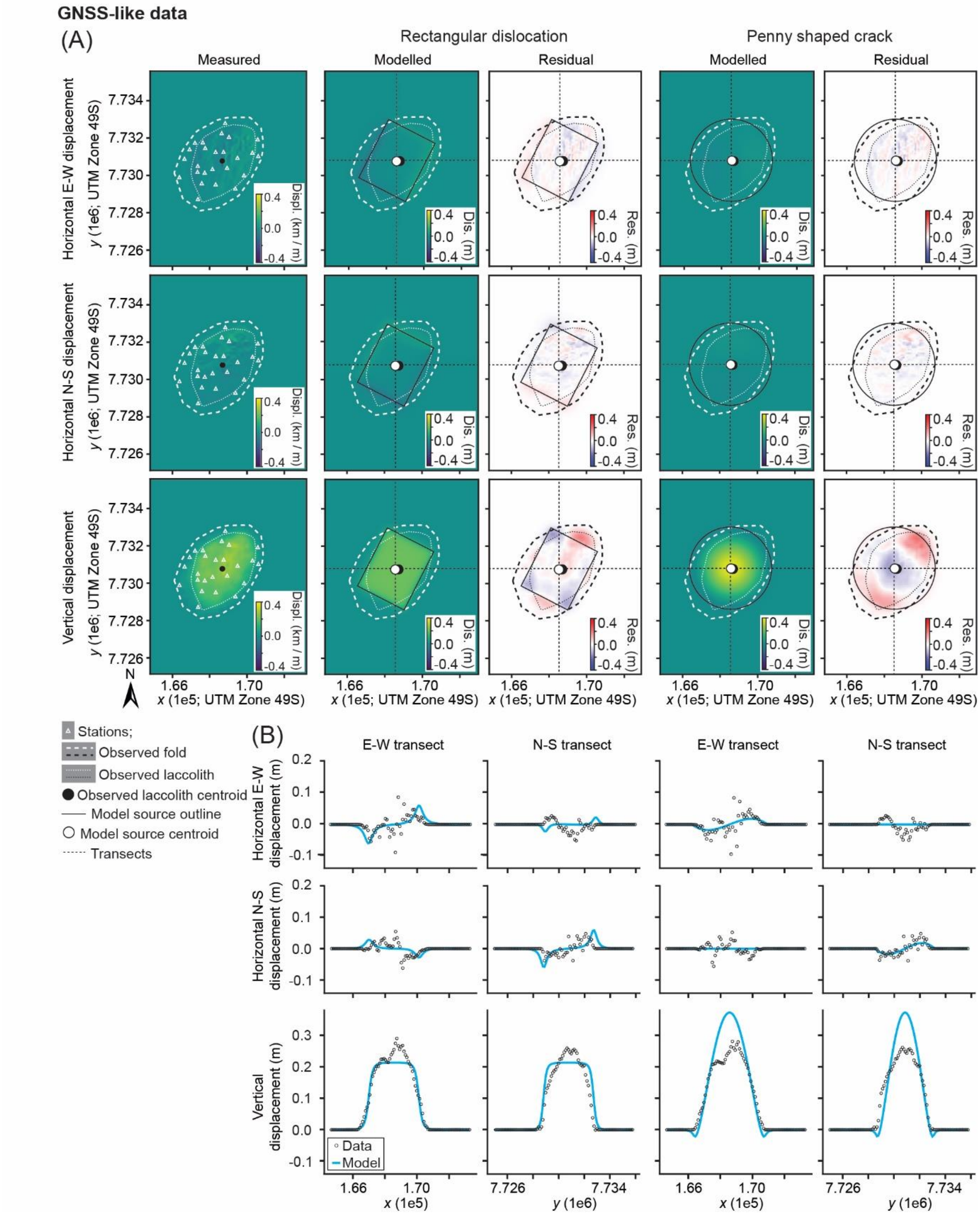

Figure 8: Map of measured U_Z and estimated U_H, highlighting the 25 stations selected for modelling, compared to forward models of the optimal scenarios derived from inverse modelling of GNSS-like data. Residual map highlights the difference to measured

displacement (displ.). (B) Transects oriented E-W and N-S through the area (see maps for locations) are also provided to compare measured and modelled displacement.

5. Discussion

5.1 Burial-related compaction and intrusion-fold discrepancies

If space for magma emplacement is solely generated by overburden uplift, we may expect the location, shape, and size of the produced forced fold and its associated surface deformation to relate simply to that of the intrusion (e.g., Galland and Scheibert, 2013). The current maximum amplitude ($f_{\max}$) of our studied forced fold at Horizon 2 is ~191–268 m (Dobb et al., 2022). Given the maximum laccolith thickness ($t_{\max}$) is ~504–617 m, the ratio $f_{\max}/t_{\max}$ is ~0.31–0.53 (Fig. 9). Seismic reflection-based studies of other intrusions have recognised similar $f_{\max}/t_{\max}$ relationships, some with $f_{\max}/t_{\max}$ ratios as low as ~0.15 (Fig. 9) (Hansen and Cartwright, 2006; Jackson et al., 2013; Magee et al., 2013; Magee et al., 2019). The magnitude of published $f_{\max}/t_{\max}$ values, as well as field observations, have been used to suggest other space-making mechanisms contemporaneously accommodate magma emplacement in addition to uplift (e.g., Hansen and Cartwright, 2006; Morgan et al., 2008; Schofield et al., 2012; Jackson et al., 2013; Magee et al., 2013; Magee et al., 2019). These other space-making mechanisms include: (1) compressibility of shallow, especially bubbly magma (e.g., Alshembari et al., 2022); and (2) inelastic deformation of the surrounding country rock (e.g., viscoelastic, compaction) (e.g., Bonafede et al., 1986; Morgan et al., 2008; Schofield et al., 2012; Head et al., 2019). If space for magma is partly generated by one or more of these space-making mechanisms, we may expect the relationship between the location, shape, and size of any contemporaneous surface displacement and intrusion to be more complicated (e.g., Galland, 2012; Jackson et al., 2013; Magee et al., 2013). For example, source volume and/or mass may be underestimated if surface displacements do not fully reflect the space needed to accommodate intrusion growth or pressurisation.

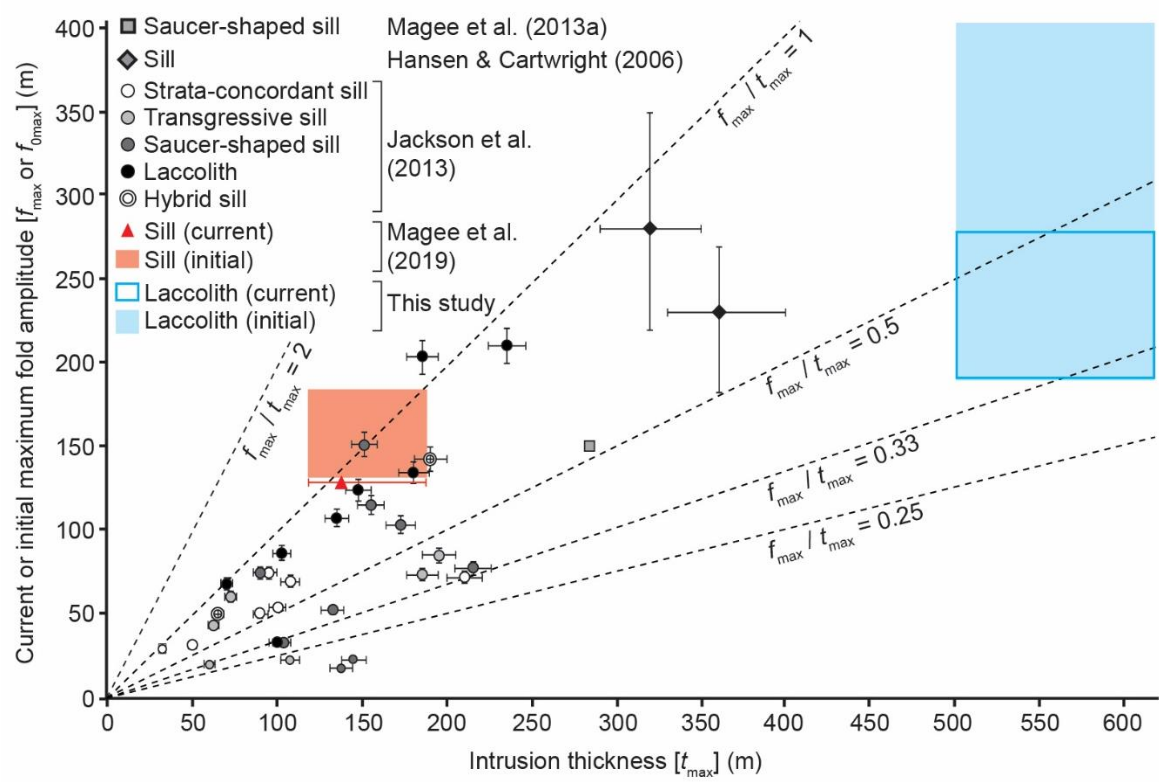

***Figure 9**: Plot comparing current maximum forced fold amplitudes (f_{max}) and maximum intrusion thicknesses (t_{max}) measured in seismic reflection data from the: (1) Bight Basin, offshore southern Australia (Jackson et al., 2013); (2) Exmouth Sub-basin, offshore north-western Australia (Magee et al., 2013); and (3) Rockall Basin, NE Atlantic (Hansen and Cartwright, 2006; Magee et al., 2019). Only Magee et al. (2019) decompacted and backstripped their data to also estimate initial maximum fold amplitudes; we follow this approach and given the uncertainties we consider present the possible range of the current and initial maximum fold amplitude.*

Most seismic-based analyses comparing intrusion and forced fold geometries and size are limited because they do not quantitatively account for: (1) burial-related compaction of the folded strata, which reduces fold amplitude but not the thickness of crystallised, (near-)incompressible intrusions, thereby causing $f_{\max} < t_{\max}$ (Magee et al., 2019); or (2) ductile strain and the upwards widening of many intrusion-induced forced folds, which to maintain their volume leads to a reduction in fold amplitude (e.g., Pollard and Johnson, 1973; Withjack et al., 1990; Hansen and Cartwright, 2006). Decompaction and backstripping techniques show estimated initial forced fold amplitudes are greater than current measurements, which in places fully accounts for $f_{\max} < t_{\max}$, i.e., $f_0 = t_0$ (e.g., Magee et al., 2019). Here, we show that the initial maximum amplitude ($f_{0\max}$) of the forced fold at Horizon 2 is ~189–402 m (Figs 4B and 9), so the ratio $f_{0\max} / t_{0\max}$ is ~0.31–0.80, assuming $t = t_0$. Indeed, across most of the fold, except its edges, $f_0 < t_0$ (Fig. 4C). With our 3D seismic reflection data, we can also calculate fold and intrusion volumes. The volume of the forced fold at Horizon 2 (~1.13–2.59 km^3) is smaller than the laccolith volume (~2.68–3.27 km^3), with the ratio between the two being ~0.35–0.97. Although errors such as changes in seismic velocity or material properties could affect our initial fold or intrusion estimates (e.g., amplitude, thickness, or volume), we adopt a conservative approach that accounts for the likely range of these uncertainties (Magee et al., 2019). We therefore have confidence that our f_0 / t_0 ratio of ~0.31–0.80 and the forced fold / intrusion volume ratio of 0.35–0.97 are real. These discrepancies in forced fold and intrusion properties can, at least partly, be explained by the recognised two-phase growth of the laccolith (Dobb et al., 2022). Specifically, the forced fold at Horizon 2 only reflects the magma volume emplaced during the second phase of intrusion, but we compare this to the cumulative laccolith thickness and volume as we cannot separate its components. However, it is also plausible that some of the discrepancies can be attributed to: (1) the expected upwards decay of fold amplitude to maintain its volume as the fold widens (e.g., Pollard and Johnson, 1973; Withjack et al., 1990; Hansen and Cartwright, 2006); and/or (2) the occurrence of other space-making mechanisms in accommodating magma emplacement (e.g., Galland, 2012; Jackson et al., 2013; Magee et al., 2013).

5.2 Testing volcano deformation models

Models represent simplifications of systems so inevitably are, to some degree, wrong (Box, 1976). We know analytical models of volcano deformation are limited by assumptions regarding intrusion geometry, material properties, and deformation behaviours (e.g., Mogi, 1958; Okada, 1985; McTigue, 1987; Fialko et al., 2001; Masterlark, 2007; Hautmann et al., 2010; Bunger and Cruden, 2011; Galland, 2012; Hickey et al., 2013; Magee et al., 2013; Hickey et al., 2016). Here, we compare source estimates derived from volcano deformation analytical solutions to an observed ancient intrusion imaged in seismic reflection data. Specifically, from our decompacted forced fold geometry, which represents the cumulative effects of laccolith growth, we model a plausible surface displacement scenario that represents a potential short-lived stage of fold growth (Fig. 1D). Our approach maintains the fold geometry and aligns with evidence that intrusion lateral extents are established early before inflation and roof uplift dominates (e.g., Cruden and McCaffrey, 2001; Karlstrom et al., 2018). However, the fit of source estimates obtained from analytical volcano deformation models will be limited by assumptions inherent to the solutions and uncertainties within our decompaction, backstripping, and scaling method.

Despite sources of error and uncertainty, our forward and inverse models produce surface displacements and source estimates that are comparable to those measured from our seismic reflection data (Figs 6-8). For example, the vertical displacement profiles obtained from some thin plate bending forward models are broadly similar (R^2 >0.5) to the observed forced fold geometry (Fig. 6; Supplementary Table 6). Inverse modelling using penny shaped crack and rectangular dislocation analytical solutions also estimates source locations and planimetric geometries that broadly fit those of the observed laccolith (Figs 6 and 7). These similarities lend confidence to both the usage of these analytical solutions, and our scaling approach for comparing surface displacement data from active and ancient systems.

There are differences between the predicted vertical and, where applicable, horizontal displacement patterns of the analytical models relative to those acquired from the seismic reflection data (Figs 6-8). For example, if pure elastic bending accommodates uplift, we expect produced forced folds to have a bell-like geometry and a power-law relationship between its amplitude and laccolith length (Figs 1B and 10A) (e.g., Pollard and Johnson, 1973; Kerr and Pollard, 1998; Galland and Scheibert, 2013). Whilst the vertical displacement profiles obtained from our thin plate bending models are bell-shaped, the observed forced fold has a prominent monoclinal rim and flatter top (Figs 2C and 6). We also find that source depths (0.16–0.41 km) derived from penny shaped crack and rectangular dislocation solutions underestimate measured emplacement depths (~0.63–1.05 km). Our range of emplacement depths estimated from the seismic reflection data accounts for uncertainty in our seismic interpretation and decompaction method. We thus have some confidence that this underestimate of ~0.22–0.89 km highlights a potential limitation of the penny shaped crack and rectangular dislocation models. In comparison, previous elastic half-space studies have found point source (Mogi) and finite volume sphere analytical solutions tend to overestimate source depths of shallow intrusions as they only work optimally when the intrusion radius-to-depth ratio is $\lesssim$0.4 or $\lesssim$0.6, respectively (Taylor et al., 2021); for context, the radius-to-depth ratio of our laccolith is ~3.6–6.0.

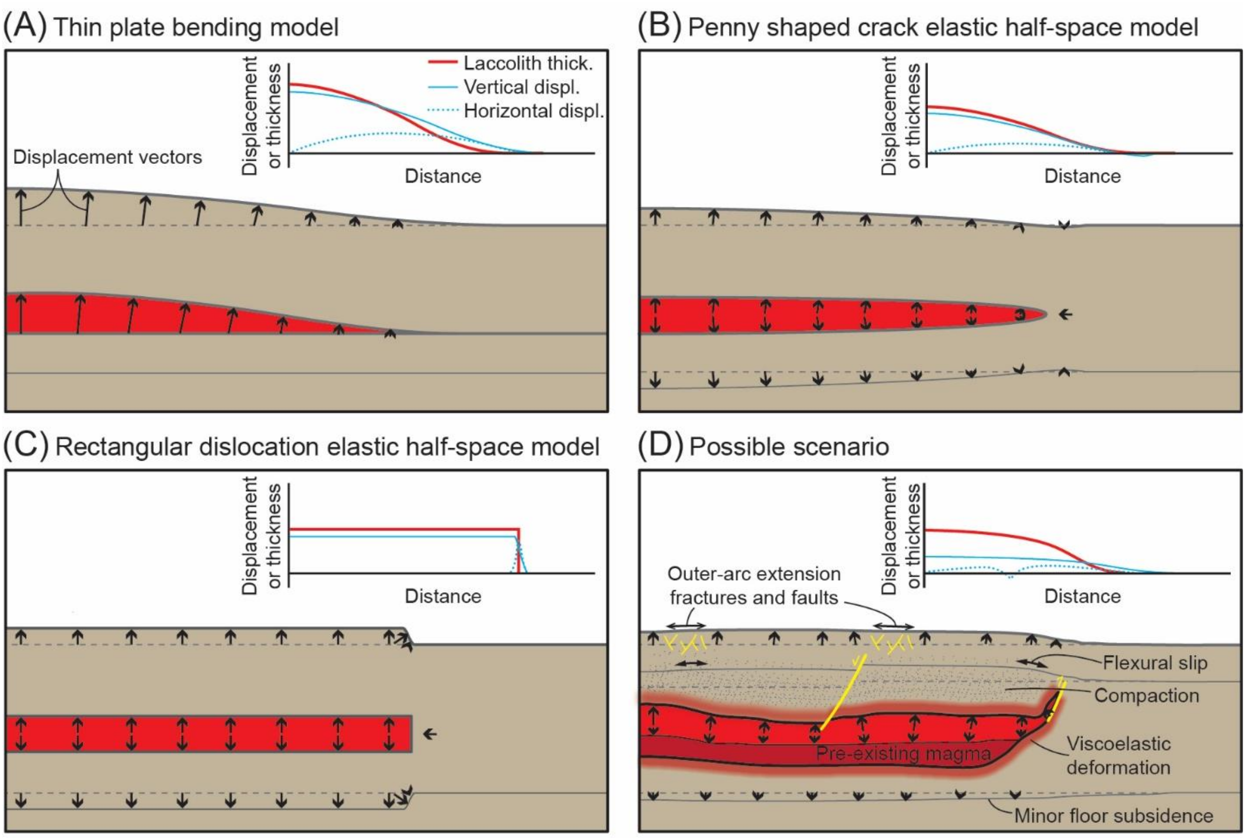

Figure 10*: Schematics showing how source deformation (i.e., magma emplacement) translates into surface displacements. Inset plots describe how vertical and horizontal surface displacements (displ.) compare to the thickness (thick.) and extent of an underlying laccolith. (A) Bending of a think elastic plate above a laccolith (Galland and Scheibert, 2013). (B) Penny shaped crack elastic half-space model (Fialko et al., 2001). (C) Rectangular dislocation elastic half-space model (Okada, 1985). (D) Likely scenario where inflation of a laccolith with a complex shape is spatially accommodated by a combination of elastic deformation, of both the roof and floor, and inelastic processes such as viscoelasticity, compaction, and those related to bending (e.g., flexural slip along rock boundaries, outer-arc extension). The occurrence of elastic and inelastic deformation means surface displacements are more decoupled from the laccolith geometry (D) than scenarios where only elastic deformation is considered (A-C).*

Variations in observed and predicted displacements probably reflect the simplicity of the analytical models, and the likelihood that displacement trajectories of surface locations were not vertical or surface-normal (cf. Figs 5B and 10). Specifically, analytical solutions cannot account for the complex geometry of natural intrusions (e.g., Galland, 2012; Poppe et al., 2024); e.g., our laccolith has neither the form of a rectangular dislocation or a penny shaped crack (Figs 2C, 4B, and 10). Nor do these analytical solutions consider how the magnitude and distribution of displacement may be influenced by: (1) complex magma dynamics (e.g., magma weight, non-uniform pressure distributions) (e.g., Bunger and Cruden, 2011); (2) host rock heterogeneity and anisotropy (e.g., layering), which changes elastic properties of rocks and for thin plate bending models reduces the elastic thickness of the overburden thereby increasing source depth estimates (e.g., Pollard and Johnson, 1973; Manconi et al., 2007; Currenti et al., 2010; Geyer and Gottsmann, 2010; Hautmann et al., 2010); or (3) contemporaneous space generation via inelastic deformation, perhaps related to extension or compression within bending layers or viscoelastic deformation adjacent to the laccolith (Fig. 10D) (e.g., Pollard and Johnson, 1973; Koch et al., 1981; Jackson and Pollard, 1990; Morgan et al., 2008; Wilson et al., 2016). Overall, it is likely a combination of elastic and inelastic processes contributes to space generation for magma, complicating its translation into surface uplift (Fig. 10D).

6. Conclusions

Modelling volcano deformation data is critical to eruption forecasting, hazard assessment, and understanding volcanic unrest because it allows us to estimate potential source geometries, locations, and conditions that can be used to infer magma supply characteristics. The application of analytical solutions is particularly widespread because they are computationally cheap and can be executed rapidly. Yet these models assume deformation sources have a simple geometry and the host material deforms elastically. Seismic reflection data offers a unique opportunity to test volcano deformation models as they can image ancient intrusions *and* overburden deformation in 3D at metre-to-decametre scales. Using seismic reflection data, we map the 3D geometry of an ancient laccolith and an overlying, dome-shaped area of uplifted strata (i.e., a forced fold) from the Exmouth Plateau, offshore NW Australia. We recover the initial, pre-burial geometry of the forced fold by decompacting and backstripping the deformed sequence using conservative estimates of material properties. Our results show that the forced fold likely had a maximum amplitude of ~189–402 m and volume of ~1.13–2.59 km^3 immediately after the final phase of magma emplacement. In contrast, the laccolith, which was emplaced at a depth of ~0.63–1.05 km, has a maximum thickness of 504–617 m, and a volume of ~2.68–3.27 km^3. The discrepancy between the fold and intrusion volumes reflects the presence of some magma prior to emplacement of the melt that instigated uplift, but also suggests other mechanisms (e.g., compaction) created space for the magma. We use thin elastic plate bending and elastic half-space, specifically penny shaped crack and rectangular dislocation, analytical solutions to forward and inverse model the recovered surface deformation of the forced fold. These models provide estimates of source (intrusion) properties that we compare to those measured directly from the seismic reflection data. To aid comparison between ancient and active magmatic systems, we scale our recovered displacement magnitudes down, whilst maintaining their spatial distribution, so they are akin to the mm–m displacements commonly observed at active volcanoes. All model estimates of laccolith size and horizontal position are reasonably similar to those measured, lending confidence to our approach. However, differences in modelled and measured surface displacements indicate the analytical solutions are limited in their ability to fit data. For example, the penny shaped crack and rectangular dislocation solutions underestimate emplacement depth by ~0.22–0.89 km. These discrepancies in source depth likely reflect the simplicity of the models relative to the heterogeneous, anisotropic, and non-linearly elastic nature of the subsurface and the processes that accommodate emplacement (e.g., other space-making mechanisms). Overall, our work emphasises the utility of seismic reflection data in helping assess the applicability of volcano deformation models.

Acknowledgements

CM, SE, and JH acknowledge funding through NERC grant NE/Y000110/1. SE is also supported by NE/R015546/1, and JH by NERC grant NE/X013944/1. We are grateful to Geoscience Australia who have made the seismic reflection and borehole data used publicly available, and to the developers of Petrel (Schlumberger), GBIS, and VSM for software provision.

Data Availability

The seismic and well data are open access and available through Geoscience Australia (http://www.ga.gov.au/nopims). The Glencoe survey and well data can also be found at: https://webapps.bgs.ac.uk/services/ngdc/accessions/index.html?simpleText=glencoe#item172421. Supplementary Table 3 provides the raw point data for all mapped horizons and their depth-converted versions, as well as the decompacted layer thicknesses they bound, which describe fold amplitude and emplacement depth, calculated for different parameter combinations. All modelling output files (e.g., logs of input parameters, convergence plots, optimal source estimates, etc…) for the thin plate bending and elastic half-space analytical solutions are provided in Supplementary Files 1 and 2. GBIS and VSM software can be accessed via https://comet.nerc.ac.uk/gbis/ and https://github.com/EliTras/VSM, respectively.

References

Allen, P. A., and Allen, J. R., 2013, Basin analysis: Principles and application to petroleum play assessment, John Wiley & Sons.

Alshembari, R., Hickey, J., Williamson, B. J., and Cashman, K., 2022, Poroelastic Mechanical Behavior of Crystal Mush Reservoirs: Insights Into the Spatio-Temporal Evolution of Volcano Surface Deformation: Journal of Geophysical Research: Solid Earth, v. 127, no. 10, p. e2022JB024332.

Bagnardi, M., and Hooper, A., 2018, Inversion of Surface Deformation Data for Rapid Estimates of Source Parameters and Uncertainties: A Bayesian Approach: Geochemistry Geophysics Geosystems, v. 19, no. 7, p. 2194-2211.

Battaglia, M., and Hill, D. P., 2009, Analytical modeling of gravity changes and crustal deformation at volcanoes: The Long Valley caldera, California, case study: Tectonophysics, v. 471, no. 1-2, p. 45-57.

Biggs, J., and Wright, T. J., 2020, How satellite InSAR has grown from opportunistic science to routine monitoring over the last decade: Nat Commun, v. 11, no. 1, p. 3863.

Bilal, A., and McClay, K., 2022, Tectonic and stratigraphic evolution of the central Exmouth Plateau, NW Shelf of Australia: Marine and Petroleum Geology, v. 136, p. 105447.

Bonafede, M., Dragoni, M., and Quareni, F., 1986, Displacement and Stress-Fields Produced by a Center of Dilation and by a Pressure Source in a Viscoelastic Half-Space - Application to the Study of Ground Deformation and Seismic Activity at Campi-Flegrei, Italy: Geophysical Journal of the Royal Astronomical Society, v. 87, no. 2, p. 455-485.

Box, G. E., 1976, Science and statistics: Journal of the American Statistical Association, v. 71, no. 356, p. 791-799.

Bunger, A. P., and Cruden, A. R., 2011, Modeling the growth of laccoliths and large mafic sills: Role of magma body forces: Journal of Geophysical Research, v. 116, no. B2.

Castro, J. M., Cordonnier, B., Schipper, C. I., Tuffen, H., Baumann, T. S., and Feisel, Y., 2016, Rapid laccolith intrusion driven by explosive volcanic eruption: Nat Commun, v. 7, p. 13585.

Chadwick Jr, W. W., Rubin, K. H., Merle, S. G., Bobbitt, A. M., Kwasnitschka, T., and Embley, R. W., 2019, Recent eruptions between 2012 and 2018 discovered at west mata submarine volcano (NE Lau Basin, SW Pacific) and characterized by new ship, AUV, and ROV data: Frontiers in Marine Science, p. 495.

Crozier, J., Karlstrom, L., Montgomery-Brown, E., Angarita, M., Cayol, V., Bato, M. G., Wang, T. A., Grapenthin, R., Shreve, T., Anderson, K., Astort, A., Bodart, O., Cannavò, F., Currenti, G., Dabaghi, F., Erickson, B. A., Garg, D., Head, M., Iozzia, A., Kim, Y. C., Le Mével, H., Lizama, C. N., Rucker, C., Silverii, F., Trasatti, E., and Zhan, Y., 2023, Understanding the drivers of volcano deformation through geodetic model verification and validation: Bulletin of Volcanology, v. 85, no. 12, p. 74.

Cruden, A. R., and McCaffrey, K. J. W., 2001, Growth of plutons by floor subsidence: Implications for rates of emplacement, intrusion spacing and melt-extraction mechanisms: Physics and Chemistry of the Earth Part a-Solid Earth and Geodesy, v. 26, no. 4-5, p. 303-315.

Currenti, G., Bonaccorso, A., Del Negro, C., Scandura, D., and Boschi, E., 2010, Elasto-plastic modeling of volcano ground deformation: Earth and Planetary Science Letters, v. 296, no. 3-4, p. 311-318.

Curtis, M. S., Holford, S. P., Schofield, N., and Bunch, M. A., 2023, Nature and preservation of Late Jurassic breakup-related volcanism in the Carnarvon Basin, North West Shelf, Australia: Marine and Petroleum Geology, v. 153, p. 106304.

Direen, N. G., Stagg, H. M. J., Symonds, P. A., and Colwell, J. B., 2008, Architecture of volcanic rifted margins: new insights from the Exmouth-Gascoyne margin, Western Australia: Australian Journal of Earth Sciences, v. 55, no. 3, p. 341-363.

Dobb, E. M., Magee, C., Jackson, C. A.-L., Lathrop, B., and Köpping, J., 2022, Impact of igneous intrusion and associated ground deformation on the stratigraphic record: Geological Society, London, Special Publications, v. 525, no. 1, p. SP525-2021-2115.

Dzurisin, D., 2006, Volcano deformation: new geodetic monitoring techniques, Springer Science & Business Media.

Ebmeier, S., Andrews, B., Araya, M., Arnold, D., Biggs, J., Cooper, C., Cottrell, E., Furtney, M., Hickey, J., and Jay, J., 2018, Synthesis of global satellite observations of magmatic and volcanic deformation: implications for volcano monitoring & the lateral extent of magmatic domains: Journal of Applied Volcanology, v. 7, no. 1, p. 2.

Fialko, Y., Khazan, Y., and Simons, M., 2001, Deformation due to a pressurized horizontal circular crack in an elastic half-space, with applications to volcano geodesy: Geophysical Journal International, v. 146, no. 1, p. 181-190.

Galland, O., 2012, Experimental modelling of ground deformation associated with shallow magma intrusions: Earth and Planetary Science Letters, v. 317, p. 145-156.

Galland, O., and Scheibert, J., 2013, Analytical model of surface uplift above axisymmetric flat-lying magma intrusions: Implications for sill emplacement and geodesy: Journal of Volcanology and Geothermal Research, v. 253, p. 114-130.

Garthwaite, M. C., Miller, V. L., Saunders, S., Parks, M. M., Hu, G., and Parker, A. L., 2019, A simplified approach to operational InSAR monitoring of volcano deformation in low-and middle-income countries: Case study of Rabaul Caldera, Papua New Guinea: Frontiers in Earth Science, v. 6, p. 240.

Geyer, A., and Gottsmann, J., 2010, The influence of mechanical stiffness on caldera deformation and implications for the 1971-1984 Rabaul uplift (Papua New Guinea): Tectonophysics, v. 483, no. 3-4, p. 399-412.

Hansen, D. M., and Cartwright, J., 2006, The three-dimensional geometry and growth of forced folds above saucer-shaped igneous sills: Journal of Structural Geology, v. 28, no. 8, p. 1520-1535.

Harmer, R., and Whelan, M., 2012, Final Well Completion Report, Chester-2: Hess Exploration Australia Pty Limited.

Hautmann, S., Gottsmann, J., Sparks, R. S. J., Mattioli, G. S., Sacks, I. S., and Strutt, M. H., 2010, Effect of mechanical heterogeneity in arc crust on volcano deformation with application to Soufriere Hills Volcano, Montserrat, West Indies: Journal of Geophysical Research-Solid Earth, v. 115, no. B9.

Head, M., Hickey, J., Gottsmann, J., and Fournier, N., 2019, The Influence of Viscoelastic Crustal Rheologies on Volcanic Ground Deformation: Insights From Models of Pressure and Volume Change: Journal of Geophysical Research-Solid Earth, v. 124, no. 8, p. 8127-8146.

Heap, M. J., Villeneuve, M., Albino, F., Farquharson, J. I., Brothelande, E., Amelung, F., Got, J. L., and Baud, P., 2020, Towards more realistic values of elastic moduli for volcano modelling: Journal of Volcanology and Geothermal Research, v. 390, p. 106684.

Hickey, J., Gottsmann, J., and del Potro, R., 2013, The large-scale surface uplift in the Altiplano-Puna region of Bolivia: A parametric study of source characteristics and crustal rheology using finite element analysis: Geochemistry Geophysics Geosystems, v. 14, no. 3, p. 540-555.

Hickey, J., Gottsmann, J., Nakamichi, H., and Iguchi, M., 2016, Thermomechanical controls on magma supply and volcanic deformation: application to Aira caldera, Japan: Sci Rep, v. 6, no. 1, p. 32691.

Hocking, R., 1992, Jurassic deposition in the southern and central North West Shelf: Western Australia: Geological Survey Western Australia Record, v. 199217.

Hocking, R. M., Moors, H. T., and Van de Graaff, W. E., 1987, Geology of the carnarvon basin, Western Australia, State Print. Division.

Jackson, C. A. L., Schofield, N., and Golenkov, B., 2013, Geometry and controls on the development of igneous sill-related forced folds: A 2-D seismic reflection case study from offshore southern Australia: Geological Society of America Bulletin, v. 125, no. 11-12, p. 1874-1890.

Jackson, M. D., and Pollard, D. D., 1990, Flexure and Faulting of Sedimentary Host Rocks during Growth of Igneous Domes, Henry Mountains, Utah: Journal of Structural Geology, v. 12, no. 2, p. 185-206.

Karlstrom, L., Richardson, P. W., O'Hara, D., and Ebmeier, S. K., 2018, Magmatic Landscape Construction: Journal of Geophysical Research-Earth Surface, v. 123, no. 8, p. 1710-1730.

Kerr, A. D., and Pollard, D. D., 1998, Toward more realistic formulations for the analysis of laccoliths: Journal of Structural Geology, v. 20, no. 12, p. 1783-1793.

Koch, F. G., Johnson, A. M., and Pollard, D. D., 1981, Monoclinal Bending of Strata over Laccolithic Intrusions: Tectonophysics, v. 74, no. 3-4, p. T21-T31.

Lai, L. S. H., Dorsey, R. J., Horng, C. S., Chi, W. R., Shea, K. S., and Yen, J. Y., 2022, Extremely rapid up-and-down motions of island arc crust during arc-continent collision: Communications Earth & Environment, v. 3, no. 1, p. 100.

Lisowski, M., 2007, Analytical volcano deformation source models, *in* Dzurisin, D., ed., Volcano deformation: Geodetic monitoring techniques: Heidelberg, Berlin, Springer, p. 279-304.

Longley, I., Buessenschuett, C., Clydsdale, L., Cubitt, C., Davis, R., Johnson, M., Marshall, N., Murray, A., Somerville, R., and Spry, T., 2002, The North West Shelf of Australia–a Woodside perspective: The sedimentary basins of Western Australia, v. 3, p. 27-88.

Magee, C., Bastow, I. D., de Vries, B. V., Jackson, C. A. L., Hetherington, R., Hagos, M., and Hoggett, M., 2017a, Structure and dynamics of surface uplift induced by incremental sill emplacement: Geology, v. 45, no. 5, p. 431-434.

Magee, C., Briggs, F., and Jackson, C. A. L., 2013, Lithological controls on igneous intrusion-induced ground deformation: Journal of the Geological Society, v. 170, no. 6, p. 853-856.

Magee, C., Hoggett, M., Jackson, C. A. L., and Jones, S. M., 2019, Burial-Related Compaction Modifies Intrusion-Induced Forced Folds: Implications for Reconciling Roof Uplift Mechanisms Using Seismic Reflection Data: Frontiers in Earth Science, v. 7, no. 37.

Magee, C., and Jackson, C. A. L., 2020, Seismic reflection data reveal the 3D structure of the newly discovered Exmouth Dyke Swarm, offshore NW Australia: Solid Earth, v. 11, no. 2, p. 579-606.

Magee, C., Jackson, C. A. L., Hardman, J. P., and Reeve, M. T., 2017b, Decoding sill emplacement and forced fold growth in the Exmouth Sub-basin, offshore northwest Australia: Implications for hydrocarbon exploration: Interpretation-a Journal of Subsurface Characterization, v. 5, no. 3, p. Sk11-Sk22.

Magee, C., Maharaj, S. M., Wrona, T., and Jackson, C. A. L., 2015, Controls on the expression of igneous intrusions in seismic reflection data: Geosphere, v. 11, no. 4, p. 1024-1041.

Magee, C., Stevenson, C. T. E., Ebmeier, S. K., Keir, D., Hammond, J. O. S., Gottsmann, J. H., Whaler, K. A., Schofield, N., Jackson, C. A. L., Petronis, M. S., O'Driscoll, B., Morgan, J., Cruden, A., Vollgger, S. A., Dering, G., Micklethwaite, S., and Jackson, M. D., 2018, Magma Plumbing Systems: A Geophysical Perspective: Journal of Petrology, v. 59, no. 6, p. 1217-1251.

Manconi, A., Walter, T. R., and Arnelung, F., 2007, Effects of mechanical layering on volcano deformation: Geophysical Journal International, v. 170, no. 2, p. 952-958.

Masterlark, T., 2007, Magma intrusion and deformation predictions: Sensitivities to the Mogi assumptions: Journal of Geophysical Research-Solid Earth, v. 112, no. B6.

Masterlark, T., Haney, M., Dickinson, H., Fournier, T., and Searcy, C., 2010, Rheologic and structural controls on the deformation of Okmok volcano, Alaska: FEMs, InSAR, and ambient noise tomography: Journal of Geophysical Research-Solid Earth, v. 115, no. B2.

McTigue, D. F., 1987, Elastic Stress and Deformation near a Finite Spherical Magma Body - Resolution of the Point-Source Paradox: Journal of Geophysical Research-Solid Earth and Planets, v. 92, no. B12, p. 12931-12940.

Menand, T., 2008, The mechanics and dynamics of sills in layered elastic rocks and their implications for the growth of laccoliths and other igneous complexes: Earth and Planetary Science Letters, v. 267, no. 1-2, p. 93-99.

Mogi, K., 1958, Relations between the eruptions of various volcanoes and the deformations of the ground surfaces around them: Bulletin of the Earthquake Research Institute, v. 36, p. 99-134.

Morgan, S., Stanik, A., Horsman, E., Tikoff, B., de Saint Blanquat, M. D., and Habert, G., 2008, Emplacement of multiple magma sheets and wall rock deformation: Trachyte Mesa intrusion, Henry Mountains, Utah: Journal of Structural Geology, v. 30, no. 4, p. 491-512.

Nikkhoo, M., Walter, T. R., Lundgren, P. R., and Prats-Iraola, P., 2016, Compound dislocation models (CDMs) for volcano deformation analyses: Geophysical Journal International, p. ggw427.

Norcliffe, J., Magee, C., Jackson, C., Kopping, J., and Lathrop, B., 2021, Fault inversion contributes to ground deformation above inflating igneous sills: Volcanica, v. 4, no. 1, p. 1-21.

Okada, Y., 1985, Surface Deformation Due to Shear and Tensile Faults in a Half-Space: Bulletin of the Seismological Society of America, v. 75, no. 4, p. 1135-1154.

Parks, M., Sigmundsson, F., Drouin, V., Hjartardóttir, Á. R., Geirsson, H., Hooper, A., Vogfjörd, K. S., Ófeigsson, B. G., Hreinsdóttir, S., and Jensen, E. H., 2023, Deformation, seismicity, and monitoring response preceding and during the 2022 Fagradalsfjall eruption, Iceland: Bulletin of Volcanology, v. 85, no. 10, p. 60.

Paumard, V., Bourget, J., Payenberg, T., Ainsworth, R. B., George, A. D., Lang, S., Posamentier, H. W., and Peyrot, D., 2018, Controls on shelf-margin architecture and sediment partitioning during a syn-rift to post-rift transition: Insights from the Barrow Group (Northern Carnarvon Basin, North West Shelf, Australia): Earth-Science Reviews, v. 177, p. 643-677.

Planke, S., Rasmussen, T., Rey, S. S., and Myklebust, R., 2005, Seismic characteristics and distribution of volcanic intrusions and hydrothermal vent complexes in the Vøring and Møre basins, *in* Doré, A. G., ed., Petroleum Geology: North-West Europe and

Global Perspectives - Proceddings of the 6th Petroleum Geology Conference, Geological Society, London, p. 833-844.

Pollard, D. D., and Johnson, A. M., 1973, Mechanics of growth of some laccolithic intrusions in the Henry Mountains, Utah, II: bending and failure of overburden layers and sill formation: Tectonophysics, v. 18, no. 3, p. 311-354.

Poppe, S., Wauthier, C., and Fontijn, K., 2024, Inversions of Surface Displacements in Scaled Experiments of Analog Magma Intrusion: Geophysical Research Letters, v. 51, no. 8, p. e2023GL106805.

Reeve, M. T., Jackson, C. A. L., Bell, R. E., Magee, C., and Bastow, I. D., 2016, The stratigraphic record of prebreakup geodynamics: Evidence from the Barrow Delta, offshore Northwest Australia: Tectonics, v. 35, no. 8, p. 1935-1968.

Reeve, M. T., Magee, C., Jackson, C. A. L., Bell, R. E., and Bastow, I. D., 2022, Stratigraphic record of continental breakup, offshore NW Australia: Basin Research, v. 34, no. 3, p. 1220-1243.

Reeves, J., Magee, C., and Jackson, C. A. L., 2018, Unravelling intrusion-induced forced fold kinematics and ground deformation using 3D seismic reflection data: Volcanica, v. 1, no. 1, p. 1-17.

Reynolds, P., Holford, S., Schofield, N., and Ross, A., 2017, The shallow depth emplacement of mafic intrusions on a magma-poor rifted margin: An example from the Bight Basin, southern Australia: Marine and Petroleum Geology, v. 88, p. 605-616.

Rohrman, M., 2013, Intrusive large igneous provinces below sedimentary basins: An example from the Exmouth Plateau (NW Australia): Journal of Geophysical Research-Solid Earth, v. 118, no. 8, p. 4477-4487.

Scheibert, J., Galland, O., and Hafver, A., 2017, Inelastic deformation during sill and laccolith emplacement: Insights from an analytic elastoplastic model: Journal of Geophysical Research: Solid Earth, v. 122, no. 2, p. 923-945.

Schofield, N. J., Brown, D. J., Magee, C., and Stevenson, C. T., 2012, Sill morphology and comparison of brittle and non-brittle emplacement mechanisms: Journal of the Geological Society, v. 169, no. 2, p. 127-141.

Segall, P., 2010, Earthquake and volcano deformation, Princeton University Press.

-, 2013, Volcano deformation and eruption forecasting: Geological Society, London, Special Publications, v. 380.

Sigmundsson, F., Parks, M., Pedersen, R., Jónsdóttir, K., Ófeigsson, B. G., Grapenthin, R., Dumont, S., Einarsson, P., Drouin, V., and Heimisson, E. R., 2018, Magma movements in volcanic plumbing systems and their associated ground deformation and seismic patterns, *in* Burchardt, S., ed., Volcanic and igneous plumbing systems, Elsevier, p. 285-322.

Skogly, O., 1998, Seismic characterization and emplacement of intrusives in the Vøring BasinM.Sc. Thesis]: University of Oslo.

Smallwood, J. R., 2009, Back-stripped 3D seismic data: A new tool applied to testing sill emplacement models: Petroleum Geoscience, v. 15, no. 3, p. 259-268.

Sparks, R. S., Biggs, J., and Neuberg, J. W., 2012, Geophysics. Monitoring volcanoes: Science, v. 335, no. 6074, p. 1310-1311.

Sparks, R. S. J., 2003, Forecasting volcanic eruptions: Earth and Planetary Science Letters, v. 210, no. 1-2, p. 1-15.

Stagg, H., Alcock, M., Bernardel, G., Moore, A., Symonds, P., and Exon, N., 2004, Geological framework of the outer Exmouth Plateau and adjacent ocean basins, Geoscience Australia.

Stearns, D. W., 1978, Faulting and forced folding in the Rocky Mountains foreland: Geological Society of America Memoirs, v. 151, p. 1-38.

Symonds, P. A., Planke, S., Frey, O., and Skogseid, J., 1998, Volcanic evolution of the Western Australian Continental Margin and its implications for basin development: The Sedimentary Basins of Western Australia 2: Proc. of Petroleum Society Australia Symposium, Perth, WA.

Taylor, N. C., Johnson, J. H., and Herd, R. A., 2021, Making the most of the Mogi model: Size matters: Journal of Volcanology and Geothermal Research, v. 419, p. 107380.

Tian, W., Li, X. M., and Wang, L., 2021, Forced Fold Amplitude and Sill Thickness Constrained by Wireline and 3-D Seismic Data Suggest an Elastic Magma-Induced Deformation in Tarim Basin, NW China: Minerals, v. 11, no. 3, p. 293.

Timoshenko, S., and Woinowsky-Krieger, S., 1959, Theory of plates and shells, McGraw-hill New York.

Tindale, K., Newell, N., Keall, J., and Smith, N., Structural evolution and charge history of the Exmouth Sub-basin, northern Carnarvon Basin, Western Australia, *in* Proceedings The Sedimentary Basins of Western Australia 2: Proc. of Petroleum Society Australia Symposium, Perth, WA1998, p. 473-490.

Trasatti, E., 2022, Volcanic and Seismic Source Modeling: An Open Tool for Geodetic Data Modeling: Frontiers in Earth Science, v. 10, p. 917222.

Trude, J., Cartwright, J., Davies, R. J., and Smallwood, J., 2003, New technique for dating igneous sills: Geology, v. 31, no. 9, p. 813-816.

van Wyk de Vries, B., Márquez, A., Herrera, R., Bruña, J. G., Llanes, P., and Delcamp, A., 2014, Craters of elevation revisited: forced-folds, bulging and uplift of volcanoes: Bulletin of Volcanology, v. 76, no. 11, p. 1-20.

Wang, C., Sun, Q. L., and Xie, X. N., 2022, Sediment deformation triggered by underlying magma intrusion: Journal of Asian Earth Sciences, v. 225, p. 105045.

Willcox, J., and Exon, N. J. T. A. J., 1976, The regional geology of the Exmouth Plateau, v. 16, no. 1, p. 1-11.

Wilson, P. I. R., McCaffrey, K. J. W., Wilson, R. W., Jarvis, I., and Holdsworth, R. E., 2016, Deformation structures associated with the Trachyte Mesa intrusion, Henry Mountains, Utah: Implications for sill and laccolith emplacement mechanisms: Journal of Structural Geology, v. 87, p. 30-46.

Withjack, M. O., Olson, J., and Peterson, E., 1990, Experimental models of extensional forced folds (1): Aapg Bulletin, v. 74, no. 7, p. 1038-1054.